

Alma Mater Studiorum Università di Bologna  
Archivio istituzionale della ricerca

On the surface energy balance closure at different temporal scales

This is the final peer-reviewed author's accepted manuscript (postprint) of the following publication:

*Published Version:*

Grachev A.A., Fairall C.W., Blomquist B.W., Fernando H.J.S., Leo L.S., Otarola-Bustos S.F., et al. (2020). On the surface energy balance closure at different temporal scales. AGRICULTURAL AND FOREST METEOROLOGY, 281, 1-17 [10.1016/j.agrformet.2019.107823].

*Availability:*

This version is available at: <https://hdl.handle.net/11585/788471> since: 2021-01-13

*Published:*

DOI: <http://doi.org/10.1016/j.agrformet.2019.107823>

*Terms of use:*

Some rights reserved. The terms and conditions for the reuse of this version of the manuscript are specified in the publishing policy. For all terms of use and more information see the publisher's website.

This item was downloaded from IRIS Università di Bologna (<https://cris.unibo.it/>).  
When citing, please refer to the published version.

(Article begins on next page)

This is the final peer-reviewed accepted manuscript of:

Andrey A. Grachev, Christopher W. Fairall, Byron W. Blomquist, Harindra J.S. Fernando, Laura S. Leo, Sebastián F. Otárola-Bustos, James M. Wilczak, Katherine L. McCaffrey, *On the surface energy balance closure at different temporal scales*, Agricultural and Forest Meteorology, Volume 281, 2020, 107823.

The final published version is available online at:  
<https://doi.org/10.1016/j.agrformet.2019.107823>

#### Rights / License:

The terms and conditions for the reuse of this version of the manuscript are specified in the publishing policy. For all terms of use and more information see the publisher's website.

This item was downloaded from IRIS Università di Bologna (<https://cris.unibo.it/>)

**When citing, please refer to the published version.**

# On the surface energy balance closure at different temporal scales

Andrey A. Grachev<sup>a, b, \*</sup>, Christopher W. Fairall<sup>a</sup>, Byron W. Blomquist<sup>a, b</sup>,  
Harindra J. S. Fernando<sup>c</sup>, Laura S. Leo<sup>c</sup>, Sebastián F. Otárola-Bustos<sup>c</sup>,  
James M. Wilczak<sup>a</sup>, Katherine L. McCaffrey<sup>a, b, 1</sup>

<sup>a</sup>NOAA Earth System Research Laboratory, 325 Broadway, R/PSD3, Boulder, CO 80305-3337, USA

<sup>b</sup>Cooperative Institute for Research in Environmental Sciences, University of Colorado, Boulder, CO, USA

<sup>c</sup>Department of Civil & Environmental Engineering & Earth Sciences, University of Notre Dame, Notre Dame, IN, USA

\* *Corresponding author. E-mail address:* Andrey.Grachev@noaa.gov (Andrey A. Grachev)

<sup>1</sup> Now at: S & P Global Market Intelligence, Boulder, CO, USA

---

## Agricultural and Forest Meteorology

AGRFORMET-D-19-00569

Manuscript submitted: 25 May 2019

Major Revisions: 14 September 2019

Minor Revisions: 18 October 2019

## Abstract

Measurements of the surface energy fluxes (turbulent and radiative) and other ancillary atmospheric/soil parameters made in the Columbia River Basin (Oregon) in an area of complex terrain during a 10-month long portion of the second Wind Forecast Improvement Project (WFIP 2) field campaign are used to study the surface energy budget (SEB) and surface fluxes over different temporal scales. This study analyzes and discusses SEB closure based on half-hourly, daily, monthly, seasonal, and sub-annual (~10-month) temporal averages. The data were collected over all four seasons for different states of the underlying ground surface (dry, wet, and frozen). Our half-hourly direct measurements of energy balance show that the sum of the turbulent sensible and latent heat fluxes systematically underestimate positive net radiation by around 20-30% during daytime and overestimate negative net radiation at night. This imbalance of the surface energy budget is comparable to other terrestrial sites. However, on average, the residual energy imbalance is significantly reduced at daily, weekly, and monthly averaging timescales, and moreover, the SEB can be closed for this site within reasonable limits on seasonal and sub-annual timescales (311-day averaging for the entire field campaign dataset). Increasing the averaging time to daily and longer time intervals substantially reduces the ground heat flux and storage terms, because energy locally entering the soil, air column, and vegetation in the morning is released in the afternoon and evening. Averaging on daily to sub-annual timescales also reduces random instrumental measurement errors and other uncertainties as well as smooths out a hysteresis effect (phase lag) in the SEB relationship between different components. This study shows that SEB closure is better for dry soils compared to wet soils and the statistical dependence of the turbulent fluxes and net radiation for freezing soil surfaces

65 appears weak, if not non-existent, apparently due to lack of the latent heat of fusion term in the  
66 traditional SEB equation.

67

68 **Keywords:** Energy balance closure • Radiative fluxes • Surface energy budget • Time  
69 averaging • Turbulent fluxes

70

## 1. Preamble

Surface energy fluxes (turbulent, radiative, and ground heat) are important in a wide variety of applications including climate modelling, weather forecasting, land-atmosphere simulations, agricultural and forestry research, and environmental impact studies. A direct application of the surface energy fluxes is the net surface energy budget (SEB). Energy balance closure including all components of the SEB at the air-surface interface is necessary for a better understanding of the atmosphere-surface exchange mechanisms and to improve models over representative areas and yearly timescales.

Surface energy balance closure is a formulation of the conservation of energy principle (the first law of thermodynamics). In other words, the SEB equation is a statement of how the net radiation is balanced by turbulent sensible, latent, and soil heat fluxes in the absence of other energy sources and sinks. Comprehensive SEB studies have been conducted since the 1950-60s (e.g., Lettau and Davidson 1957; Long et al. 1964). Since the late 1980s, it has become obvious that the surface energy balance is difficult to close at temporal scales less than several hours (e.g., at half-hourly and hourly averaged time scales) as reported in many studies (e.g., Wilson et al. 2002; Foken et al. 2006; Mauder et al. 2007; Oncley et al. 2007; Cava et al. 2008; Foken 2008; Jacobs et al. 2008; Panin and Bernhofer 2008; Higgins 2012; Leuning et al. 2012; Stoy et al. 2013; Cuxart et al. 2015; Majozi et al. 2017; Gao et al. 2017a and references therein).

According to field measurements, the sum of the turbulent fluxes of sensible and latent heat plus the ground heat flux in most cases (generally during daytime) is systematically smaller than that required to balance the net radiation; whereas this sum generally overestimate the net radiation at night. The lack of energy balance closure at half-hourly and hourly measurements is a

fundamental and pervasive problem in micrometeorology. Note, however, that in some cases the authors reported that the energy budget can be closed within reasonable limits (e.g., Lamaud et al. 2001; Jacobs et al. 2008), but these successes are rare.

This study utilizes the data of surface fluxes (turbulent and radiative) and other ancillary atmospheric and soil data collected in the Columbia River Gorge area near Wasco, Oregon, during a 10-month long period within the second Wind Forecast Improvement Project (WFIP 2) from 24 June 2016 through 1 May 2017 (year days 176–487 with respect to 1 January 2016). The WFIP 2 project is a four-year multi-disciplinary effort intended to improve short-term weather forecast models and better understand various unresolved physical processes that affect wind energy generation in regions of complex terrain such as coastlines, mountains, and canyons, in order to develop and evaluate improved surface-flux parameterizations (see Bianco et al. 2019; Olson et al. 2019; Shaw et al. 2019; Wilczak et al. 2019 for details). The observational phase of the WFIP 2 allows for an analysis of the SEB for different soils over a broad range of temporal scales based on first principles.

The main objectives of this study are twofold. The first objective is an investigation of the non-closure of the SEB for three different type of soils (dry, wet, and frozen surfaces) using the same instruments, experimental setup, location, and data processing. The second objective is an analysis of SEB closure at different temporal scales from half-hourly to daily and even monthly, seasonal and sub-annual averaged time series. In some sense, this study bridges micrometeorological measurements and climatological timescales through temporal averaging. The layout of the paper is as follows. The theoretical background (basic SEB equations) and the energy balance closure problem are considered in Section 2. Instruments, data collection and site descriptions are documented in Section 3. Main findings of the study based on analysis of the

WFIP 2 experimental data (e.g., time series, SEB at different timescales, and over different types of soil surfaces) are described in Section 4. The conclusions are summarized in Section 5.

## 2. The Surface Energy Balance Closure Problem

The law of conservation of energy at the interface between atmosphere and land in the absence of other energy sources and sinks is written as:

$$H_S + H_L + G = R_{net} \quad (1)$$

where  $G$  is the soil heat flux,  $R_{net}$  is the net radiation defined as the balance between downwelling (incoming) and upwelling (outgoing) SW and LW radiation:

$$R_{net} = SW_{down} - SW_{up} + LW_{down} - LW_{up} \quad (2)$$

The turbulent fluxes of sensible heat  $H_S$  and latent heat  $H_L$  in (1) can be estimated by the eddy correlation method according to

$$H_S = c_p \rho \overline{w' \theta'} \quad (3)$$

$$H_L = \mathcal{L}_e \rho \overline{w' q'} \quad (4)$$

where  $\rho$  is the mean air density,  $\theta$  is the air potential temperature,  $q$  is the air specific humidity,  $c_p$  is the specific heat capacity of air at constant pressure, and  $\mathcal{L}_e$  is the latent heat of evaporation of water. Here  $w$  is the vertical velocity component, the prime  $[']$  denotes fluctuations about the mean value, and an overbar is an averaging operator (half an hour in this study).

As mentioned above, numerous direct measurements of all SEB components in (1) have shown that over land the sum  $H_S + H_L + G$  in most cases (generally during daytime) systematically underestimate the net radiation  $R_{net}$  by about 20-30% (Foken and Oncley 1995; Wilson et al. 2002; Meyers and Hollinger 2004; Foken et al. 2006; Mauder et al. 2007; Cava et

al. 2008; Foken 2008; Jacobs et al. 2008; Panin and Bernhofer 2008; Higgins 2012; Leuning et al. 2012; Stoy et al. 2013; Masseroni et al. 2014; Gao et al. 2017a).

Because the energy balance at the surface often cannot be closed based on experimental observations, the SEB equation (1) is typically formulated as (e.g., Foken et al. 2006):

$$H_S + H_L + G + Res = R_{net} \quad (5)$$

where  $Res$  is any residual term (imbalance). Equation (1) assumes an ideal case, when all the fluxes are measured at the infinitesimal interface between an atmosphere and a soil, while Eq. (5) implies a two-layer (atmosphere and soil) column of finite thickness (e.g., Foken 2008, Fig. 1). The turbulent and soil fluxes in (5) are measured at the upper and lower boundary planes of the total layer respectively. Clearly a variety of factors may be responsible for the lack of SEB closure in the layer (e.g., Foken et al. 2006; Mauder et al. 2007; Higgins 2012; Leuning et al. 2012). Therefore, in general  $Res$  can be partitioned as:

$$Res = T + S + X \quad (6)$$

where  $T$  is an additional transport (vertical and horizontal) through all boundary planes,  $S$  is a total storage in the two-layer column, and  $X$  indicates all other unspecified contributions to (1).

The additional transport term  $T$  in (6) includes the divergence of the horizontal turbulent flux caused by complex terrain or heterogeneities in the underlying surface and soil heat transfer by convection or circulation (in addition to conductive heat flux  $G$ ) and/or by convective water flux in the water-saturated soils at the bottom plane (the water flux in the soil is a consequence of the law of conservation of mass in the case  $H_L \neq 0$ ). The storage term,  $S$ , can be partitioned as (e.g., Meyers and Hollinger 2004; Oncley et al. 2007; Leuning et al. 2012; Masseroni et al. 2014):

$$S = S_a + S_g + S_p + S_c + S_x \quad (7)$$

Where  $S_a$  is storage of energy in the air column due to radiative and/or sensible heat flux divergence (the air enthalpy change),  $S_g$  is the ground heat storage above a heat flux plate measurement level,  $S_p$  is the radiation consumed in photosynthesis (the photosynthesis flux),  $S_c$  is the canopy heat storage in biomass (the rate change in enthalpy of the vegetation), and  $S_x$  is all other storage terms, e.g. the atmospheric moisture change and the canopy dew water enthalpy change (Jacobs et al. 2008). The term  $X$  in Eq. (6) may include several factors: loss of low-frequency covariance contributions to the turbulent fluxes induced by insufficient averaging time and/or inadequate resolution of high-frequency flux components; choice of coordinate systems; the mismatch between the footprint of the turbulent heat fluxes and the measurements of radiation components and soil heat fluxes; instrumental errors; the latent heat of fusion term (see below); etc. The lack of SEB closure raises concerns regarding eddy covariance measurements at standard half-hourly and hourly averaging time scales. There are suggestions that increasing the turbulence averaging time can improve SEB closure by capturing additional sensible and latent heat fluxes at low-frequencies (e.g., Foken 2008).

Recall that failure to close the energy balance is associated with a systematic bias. Specifically, for a positive net radiation,  $R_{net} > 0$  (generally during daytime), the left-hand side of Eq. (1) is routinely smaller than the right-hand side ( $Res > 0$  in Eq. (5)) and vice versa for a negative net radiation,  $R_{net} < 0$  (generally during night). An immediate problem for the additional terms (6) is that the different terms contribute differently (either positively or negatively) to the bias. While all the storage terms (7) and the loss of high-frequency components in the turbulent fluxes contribute positively to  $Res$  in the case  $R_{net} > 0$ , it is difficult to see why the loss of low-frequency covariance associated with local circulations would always lead to an underestimation of the turbulent fluxes, and the same could be said about advection

(Finnigan 2008). For example, according to SHEBA data (Grachev et al. 2005, Fig. 8), the low-frequency flux components can be both positive and negative. Thus, while the storage term  $S$  in Eq. (6) is always positive (systematic contribution) for the positive net radiation, the other two terms,  $T$  and  $X$ , contribute positively or negatively to the bias (random contribution).

The various terms in Eq. (1) differ greatly in magnitude. Generally the soil heat flux  $G$  is relatively small compared with the net radiation, but in some cases the  $G$  term in Eq. (1) cannot be ignored. Magnitude of the ratio  $G/R_{net}$  will typically vary between 0.05 and 0.50, depending on the period of the day, thermal properties of the soil, surface cover, soil moisture content, and solar irradiance (Kustas et al. 1993). For example, midday values of the ratio of the soil heat flux and the net radiation,  $G/R_{net}$ , are about 0.15 for measurements over fields of bare soil, alfalfa, and cotton near Phoenix, AZ according to Kustas and Daughtry (1990), and 0.14-0.17 for a no-till cornfield in central Iowa in November (Sauer et al. 1998). During the night or in the fall/winter,  $G$  is an important term in (1), when  $R_{net}$  is low and stable atmospheric conditions cause  $H_S$  and  $H_L$  to be small. Despite its relative importance, the soil heat flux is not often measured, including this study where the observational site was not instrumented with a heat flux plate (e.g., see survey in Liebethal et al. 2005; Liebethal and Foken 2007; Gao et al. 2017b; Yang and Wang 2008).

The soil heat flux can be estimated from soil temperature profile measurements using Fourier's Law of Heat Conduction (gradient method)

$$G(z) = -\lambda \frac{\partial T_s}{\partial z} \quad (8)$$

where  $\lambda$  is the thermal conductivity of the soil and  $\partial T_s / \partial z$  is the vertical temperature gradient of the soil temperature,  $T_s$ . In practical applications the first derivative of the soil temperature in (8) is usually replaced by the finite-difference approximation in the soil layer  $\Delta z$  and Eq. (8) reduces

to  $G(z) \approx -\lambda \Delta T_s / \Delta z$ . Fourier's Law (8) presumes steady state heat conduction, one-dimensional heat flow, an isotropic and homogeneous material, constant thermal conductivity  $\lambda$ , and no internal heat generation. Generally, soil is a three-phase material (water, air, solid) and application of Eq. (8) is considerably more difficult. The thermal conductivity of soil depends on the conductivity of each phase and their proportions; that is,  $\lambda$  varies by composition of the solid fraction (e.g., mineral type and particle size), water content (thermal conductivity of water is about two to three times greater than that of soil), amount of organic matter, and bulk density. As a result,  $\lambda$  values can change between layers within  $\Delta z$  even for the same soil due to changes in water content. Another complexity of the gradient method (8) is associated with non-stationarity (diurnal variations), even during a half-hour averaging period. The diurnal cycle of solar radiation modulates a sinusoidal variation in the ground surface heat flux and diurnal thermal waves in the top soil layer. The temperature wave damps exponentially with depth and its lag time increases with depth. The ground heat flux is theoretically  $\pi/4$  (1/8 cycle) out of phase with the temperature wave (hysteresis effect); that is, the ground heat flux is largest three hours ahead of the surface temperature for a diurnally varying surface temperature cycle (Arya 1988; Garratt 1992; Gao et al. 2010). Thus, while the gradient method (8) is simple to employ under field conditions, accurate measurement of  $\lambda$  and the vertical soil temperature gradient is challenging. The impact of the hysteresis effect in diurnal cycles and the effect of the wave phase difference between different atmospheric and/or soil variables on the SEB closure are discussed in number of studies (e.g., Gao et al. 2010, 2017a; Sun et al. 2013).

Direct measurements of the turbulent flux of carbon dioxide allow estimation of a storage term  $S_p$  in (7) associated with the photosynthesis flux. The photosynthesis flux  $S_p$  is the change in the Gibbs free energy and, according to Nobel (2009, Chapter 6.5, p. 313), about 479 kJ of

energy is stored per mole of  $\text{CO}_2$  fixed into photosynthetic products; that is,  $S_p [\text{W m}^{-2}] = -0.479$   
 $F_{\text{CO}_2} [\mu\text{mol m}^{-2} \text{s}^{-1}]$ . For example, a canopy assimilation rate of  $F_{\text{CO}_2} = 10 \mu\text{mol m}^{-2} \text{s}^{-1}$  equates to  
energy flux of  $S_p = 4.79 \approx 5 \text{ W m}^{-2}$  (cf., Meyers and Hollinger 2004, their Fig. 5 and Masseroni  
et al. 2014, their Fig. 3). Thus, the photosynthesis storage term is relatively small; according to  
estimate by Finnigan (2008),  $S_p \approx 0.01 R_{\text{net}}$ . The canopy heat storage term (e.g., because of  
changes in leaf temperature),  $S_c$ , may be also a factor in the lack of closure, but it cannot be  
easily assessed and flux values cannot be easily corrected for this influence in the framework of  
our study. According to Meyers and Hollinger (2004, Figs. 4 and 5) and Masseroni et al. (2014,  
Fig. 3), generally  $S_c \leq S_p$ . Although the soil heat flux  $G$  in Eq. (5) and the storage terms  $S_a$  and  
 $S_g$  in Eq. (7) can be estimated from the observations, their contribution to SEB closure at half-  
hourly time scales lies beyond the scope of this study.

The SEB (1) and the fact that the turbulent fluxes are highly correlated with the net  
radiation (e.g., see plots presented in Sub-section 4.3 shortly) provide an objective approach to  
estimate turbulent fluxes independently of a conventional bulk flux algorithm. Traditionally, the  
SEB is considered closed in numerical models of the climate system and in other applications  
(e.g., for remote sensing), allowing for estimation of missing terms as the residual of the others  
(e.g., Cuxart et al. 2015 and references therein). Similar ideas are used in soil-vegetation-  
atmosphere transfer schemes where  $H_S$  and  $H_L$  are estimated from thermal infra-red data (i.e.  
radiometric surface temperature) and SEB, Eq. (1) (e.g., Priestley and Taylor 1972; Su 2002;  
Kustas et al. 2004; Ezzahar et al. 2012; Yao et al. 2015 and references therein).

### 3. Observation Site and Instrumentation

Figure 1 shows the study area located along the Columbia River Gorge in eastern Oregon and Washington states. This region was chosen because of its combination of complex terrain and extensive wind farm development. These measurements provide insight into the structure and evolution of atmospheric flows and other physical processes in complex terrain leading to improvements in parametrization of subgrid-scale processes in NWP models to support wind energy forecasting (see Bianco et al. 2019; Olson et al. 2019; Shaw et al. 2019; Wilczak et al. 2019). Federal agencies, private companies, and universities collaborated on the WFIP 2 project, deploying wind profiling radars, sodars, lidars, networks of tall meteorological towers, and other instruments across a range of spatial scales (Figs. 1 and 2).

In this observational study we use measurements of half-hourly averaged turbulent and radiative fluxes, surface meteorology, and basic soil parameters from the Physics Site 1 tower (PS01, 45.64°N and 120.68°W) located near Wasco, Oregon, (Fig. 1) to examine SEB closure over different soil conditions (dry, wet, and frozen) and at different averaging timescales. Turbulent fluxes and mean meteorological data were measured continuously on a 10-m meteorological tower at two levels, nominally 3 m and 10 m (Fig. 2). Each level was instrumented with identical fast response three-axis sonic anemometers sampling wind velocity and sonic temperature at 20 Hz (R.M. Young Model 81000) and Rotronics HC2S3 temperature and relative humidity probes (T/RH, sampling frequency = 1 Hz). The HC2S3 probes were housed in ventilated radiation shields. A fast-response (20 Hz) open path infrared gas analyzer (LI-7500, LI-COR Inc.) was collocated at 3-m height with the lower sonic anemometer for direct measurements of water vapor turbulent flux and other relevant turbulent statistics. Measurements were collected by a data-logger (Campbell CR3000) and successively parsed into 15-minute data files for cell-modem network transmission to remote data storage.

Tower-based eddy covariance measurements provide a long-term near continuous temporal record of half-hourly averaged turbulent momentum, mass, and energy fluxes. The mean wind speed and wind direction were derived from the sonic anemometers, with rotation of the measurement axes to place the measured wind components in a streamline coordinate system based on half-hour averaged 20-Hz data. In this study, we performed tilt-corrections of the sonic anemometer data using the "planar-fit" method rotation of the coordinate system proposed by Wilczak et al. (2001), which essentially fits a climatological plane through the streamlines of the local flow. The planar-fit angles were calculated from 30-min averages at each level over the 10-month dataset (for the period 24 June 2016 to 01 May 2017). Several data-quality indicators based on objective and subjective methods have been applied to the original flux data to remove spurious or low-quality records. Specifically, turbulent data have been edited for unfavorable relative wind direction for which the tower was upwind of the sonic anemometers, non-stationarity, minimum or/and maximum thresholds for the turbulent statistics, etc. (e.g., Bariteau et al. 2010; Grachev et al. 2011; Grachev et al. 2015; Blomquist et al. 2014 and references therein). In particular, sonic anemometer data based on the planar-fit procedure were flagged as bad if mean vertical velocity component differed by more than  $0.2 \text{ m s}^{-1}$  from the plane.

Measurements of soil temperature and moisture were made at five levels located nominally at 5, 10, 20, 50, and 100 cm depths below the ground surface approximately 5 m from the flux tower. Campbell Scientific 107 temperature sensors and a CS616 water content reflectometer were used to measure temperature and soil moisture (in volumetric water content) respectively. No direct measurements of surface soil heat flux with a heat flux plate were performed at this site. The soils at the WFIP 2 Physics Site PS01 are primarily well-drained silt

(73%), with minor components of sand (14%), and clay (13%) and average 152 cm in depth before reaching harder rock (water table).

The downwelling and upwelling radiation was measured from two radiation masts located near the flux tower (Fig. 2). Eppley pyranometer (PSP) and pyrgeometer (PIR) are used to measure the shortwave and infrared radiation. Both 'slow'-response radiation and soil data reported here are based on raw measurements sampled at 1 Hz which were subsequently averaged over 1-min time intervals and recorded by a data-logger. The instrument suite located on the tower was operated by University of Notre Dame scientists; solar radiation and soil science instruments were conducted by the NOAA/ESRL team.

## **4. Analysis of the WFIP 2 Data**

### *4.1. Time Series*

In this sub-section, we analyze the time series of half-hour averaged surface fluxes and basic meteorological variables to describe weather and soil conditions, surface fluxes, and other relevant variables as observed during the entire WFIP 2 field campaign for the period 24 June 2016 to 01 May 2017 (Year Days 176-487 with respect to January 1, 2016 UTC). Figures 3 and 4 show the time series of 'slow' half-hourly averaged basic meteorological variables collected at the Physics Site PS01 near Wasco, Oregon (Fig. 2), except for the rain rate which was measured near another observational site located near the Wasco State Airport (WCO). Figure 5 shows the time series of short-wave (SW) and long-wave (LW) radiation (downwelling and upwelling), radiation budgets, and also the surface albedo observed at Physics Site PS01. By convention,

radiation fluxes are positive when directed toward the surface, fluxes away are negative. The net radiation describes the balance between incoming (downwelling) and outgoing (upwelling) SW and LW radiation. The surface albedo (reflectivity of a surface) in Fig. 5d is derived from the ratio of the upwelling SW radiation (i.e., reflected from the surface) to the downwelling SW radiation. Time series of the half-hour averaged friction velocity  $u_* = \sqrt{-\overline{w'u'}}$ , sensible  $H_S$  and latent  $H_L$  heat fluxes defined by Eqs. (3)–(4) are shown in Fig. 6.

Figure 3b shows that the prevailing winds have a bimodal distribution with the two dominant wind directions  $\sim 180^\circ$  apart (easterly and westerly winds). These predominant winds generally blow parallel to the ridge in the Fig.2. The air and soil temperatures display the familiar strong seasonal trend with maximum in mid-summer and minimum during winter (Figs. 3c and 4a). The seasonal pattern of the air temperature (Fig. 3c) is highly correlated with soil thaw and freeze (Figs. 4a and 5d). The onset of near-surface soil freezing occurred in the autumn on about days 343–344 (8–9 December 2016). Frozen ground started warming when the gradient of the subsurface temperature changed sign on about days 428–429 (3–4 March 2017). The air temperatures rise above freezing during spring melt on about days 424–425 (27–28 February 2017) and eventually reaches a summer maximum (Fig. 3c). The rather constant temperature of the soil at 5 and 10-cm levels near  $0^\circ\text{C}$  (Fig. 4a) on about days 344–428 (9 December 2016–3 March 2017) is due to the snow cover when present (cf. Fig. 5d), to the rather high moisture content of the soil (Fig. 4b), and to releasing latent heat of fusion of soil water as soil freezes. The near-zero topsoil temperatures on these days are due to the phase transition of water to ice and are associated with the so-called "zero-curtain" effect (e.g., Grachev et al. 2018 and reference therein). Release of latent heat during the freezing of pore water results in the maintenance of isothermal temperatures at or around  $0^\circ\text{C}$  within the freezing ground layer over

extended periods (Fig. 4a). The zero curtain decouples the soil from the atmosphere, preventing cooling in the underlying ground layer (zero soil heat flux) for its duration (e.g., see Grachev et al. 2018 Figs. 9c and 9d) and thus protecting the ground from severe freezing.

The date of the first snowfall and the occurrence of the snow-free date are determined radiometrically as the date when the surface albedo first rises above and drops below 30% respectively (Stone et al. 2002). This behaviour of the albedo around a first snowfall/melt date is associated with a distinguishing feature of the upwelling (reflected) SW solar radiation which is changes rapidly during snowfall and snowpack disintegration, i.e., during the transition from the low-albedo bare soil to snow cover and vice versa. According to Fig. 5d, the albedo increases suddenly on days 342–344 (7–9 December 2016) with the first snowfall in the vicinity of the flux tower. The date of snow melt is evidenced by the large reduction in albedo that occurs on days 425–426 (28 February–1 March 2017), i.e., when the snow cover essentially disappears (Fig. 5d). These dates of the first snowfall and snow melt are in close correspondence with the dates of the soil freezing and melt derived independently from the temperature measurements.

The annual cycle of the downwelling SW radiation  $SW_{down}$  at half-hourly resolution is clearly evident with maximum flux values in mid-summer of about 940 to 960 W m<sup>-2</sup> (Fig. 5a) and values that drop to minimum during winter months. Similarly, the downwelling longwave radiation  $LW_{down}$  reaches a minimum in winter and a maximum in summer (Fig. 5b). A net longwave radiative loss (difference between blue and red symbols in Fig. 5b) occurs throughout the year (Fig. 5c). Hence, the net radiation  $R_{net}$  is weakly negative during winter months (Fig. 5c). The peak in  $R_{net}$  occurs during spring/summer when the snow melts and the surface albedo reaches the low summertime values and  $SW_{down}$  is near the annual peak (Fig. 5).

Figure 6 shows the seasonal cycles of the friction velocity and the turbulent fluxes of the sensible heat, and latent heat at half-hourly resolution. It is obvious that friction velocity (Fig. 6a) and the wind speed (Fig. 3a) are highly correlated to one another. The annual course of the sensible heat flux and the net radiation,  $R_{net}$  are qualitatively very similar (cf. Figs. 5c and 6b) because the balance between solar and longwave radiation is the principal energy source for daytime surface warming and evaporation (see Eq. (1)). Concurrently, the annual course of the latent heat flux shown in Fig. 6c depends on both  $R_{net}$  according to Eq. (1) and soil moisture (Fig. 4a). Figure 6 shows that during the winter and cold seasons, the sensible and latent heat fluxes were small and mostly irregular when the ground is covered with snow and air temperatures are generally below freezing. However, the turbulent fluxes increase rapidly in magnitude when air temperatures rise above freezing during spring melt and eventually reach a summer maximum (cf. Figs. 3 and 6). During late summer and early autumn all turbulent fluxes rapidly decrease in magnitude when the air temperature decreases and falls below freezing.

Based on the seasonal behaviour of the surface fluxes and surface meteorology shown in Figs. 3-6 for the entire field campaign (from 24 June 2016 to 01 May 2017), we sort the data into three categories separated by threshold values deduced from the time series of soil temperature (Fig. 4a) and soil moisture at 5 cm depth (Fig. 4b). We distinguish three soil conditions (see also Figs. 4d and 6d):

- (i) Dry bare or lightly vegetated soil surfaces, the soil temperature at 5 cm depth  $> 1^{\circ}\text{C}$  and the soil moisture at 5 cm depth  $\leq 0.07$ ;
- (ii) Wet bare or lightly vegetated soil surfaces, the soil temperature at 5 cm depth  $> 1^{\circ}\text{C}$  and the soil moisture at 5 cm depth  $> 0.07$ ;
- (iii) Frozen (snow covered) soils surfaces, the soil temperature at 5 cm depth  $\leq 1^{\circ}\text{C}$ .

Soil moisture content above is measured as the ratio of the volume of liquid water to soil volume.

#### 4.2. SEB at different timescales

In this and next sub-sections, we consider, first, the incomplete the energy balance equation,  $H_S + H_L$  versus  $R_{net}$ ; that is, Eq. (1) without the ground heat flux term  $G$  since direct measurements of  $G$  (by a flux plate) were not available. Further in Sub-section 4.5 we will estimate the soil heat flux  $G$  in Eq. (1) based on the available information (soil temperature and moisture, upwelling longwave radiation) to evaluate influence of  $G$  for the "complete" SEB closure equation,  $H_S + H_L + G$  versus  $R_{net}$ , at different temporal scales for the entire dataset and separately for different soil types. Thus, the incomplete SEB closure equation (without the ground heat flux  $G$ ) is based only on the direct measurements of the surface fluxes  $H_S$ ,  $H_L$ , and  $R_{net}$ ; whereas, the "complete" SEB closure equation (with  $G$ ) is based on the direct measurements of  $H_S$ ,  $H_L$ ,  $R_{net}$  plus modelled  $G$  (indirect estimates).

The closure of the incomplete SEB during the entire field campaign is shown in Fig. 7. Fig. 7a shows a scatter plot of the sum of the sensible and latent heat fluxes versus the net radiation for half-hourly averaged fluxes. Fig. 7b presents a similar plot based on daily, monthly, and sub-annual (311 days) averages. Note that the daily, weekly, monthly etc. data points in this study are derived from the original half-hourly averaged fluxes averaged over longer time scales. Our direct measurements of SEB in Fig. 7a are roughly consistent with past eddy-covariance results over land showing that the sum of  $H_S$  and  $H_L$  systematically underestimate the net radiation for  $R_{net} > 0$  (generally during daytime convective conditions) and overestimate for  $R_{net} < 0$  (generally during nocturnal boundary layer). According to Fig. 7a, the linear regression

forced through the origin for the half-hourly data is  $y = 0.77x$  with the correlation coefficient  $R^2 = 0.94$  (number of data points,  $N = 3624$ ) in the case  $R_{net} > 0$  (dashed magenta line) and the regression is  $y = 0.27x$  with  $R^2 = 0.41$  and  $N = 897$  in the case  $R_{net} < 0$  (dotted red line). In total for both positive and negative  $R_{net}$  the linear regression forced through the origin is  $y = 0.76x$  (not shown) with  $R^2 = 0.95$  and  $N = 4521$ .

Thus, the SEB imbalance for half-hourly averaged fluxes over the entire WFIP 2 field campaign (from 24 June 2016 to 01 May 2017) is about 24%. This mean imbalance is generally consistent with other efforts to close the SEB (e.g., Foken and Oncley 1995; Wilson et al., 2002; Meyers and Hollinger 2004; Foken et al., 2006; Oncley et al. 2007; Cava et al. 2008; Foken 2008; Jacobs et al. 2008; Panin and Bernhofer 2008; Higgins 2012; Leuning et al., 2012; Stoy et al., 2013; Masseroni et al., 2014; Cuxart et al., 2015; Gao et al., 2017a). Despite multiple review papers that discuss the lack of energy closure at half-hourly and hourly averaged timescales, and the myriad of studies devoted to the investigation of the individual factors of the imbalance at these averaging period, the SEB closure at the longer averaging times (from the daily to sub-annual timescales) has not been systematically examined. In recent years, several papers (e.g., Finnigan et al. 2003; Mauder and Foken, 2006; Leuning et al. 2012; Charuchittipan et al. 2014; Reed et al. 2018) have worked to address this issue, however, there is no consensus on how to improve energy closure.

Foken et al. (2006) applied the ogive analysis to the data measured over a maize field of the LITFASS-2003 experiment and was focused mainly on data from three selected days, where the averaging time was extended up to 4 hours. According to Charuchittipan et al. (2014), extension of the averaging time by a few hours does not significantly improve the energy balance. Previous work by Leuning et al. (2012) has shown that energy closure is observed at

only 8% of flux sites in the La Thuile synthesis dataset (produced after a workshop in La Thuile, Italy, in February, 2007) with half-hourly averages but this increases up to 45% of sites using daily averages. Recent work by Reed et al. (2018) examined the effect of temporal variation in the SEB for different site locations and seasons at annual and sub-annual timescales. Here, we focus on the longer averaging time intervals than in the papers mentioned above; that is, substantially longer daily averages (up to annual timescales).

Our data shows that, in general, increasing the averaging time consistently from half-hourly to daily and longer time intervals substantially reduces the SEB imbalance. According to Fig. 7b, the linear regression forced through the origin is  $y = 0.85x$  with the correlation coefficient  $R^2 = 0.93$  ( $N = 243$ ) in the case of daily averages (green circles and dashed magenta line) and in the case monthly (30-day) averages the regression is  $y = 0.91x$  with  $R^2 = 0.99$  and  $N = 10$  (i.e., ten full months, blue triangles and dotted red line). Moreover, the SEB can be closed for this site within several percent on sub-annual timescale (red star); that is,  $\langle H_S \rangle + \langle H_L \rangle = 1.02 \langle R_{net} \rangle$  where  $\langle \dots \rangle$  denotes an averaging operator (the arithmetic mean) for all available half-hourly values of the surface energy fluxes during the entire field campaign (311-day dataset). In this case,  $N = 1$  (one data point). Given sufficient data, it would be ideal for these purposes to average half-hourly or hourly data for a full year without large gaps (365-day averaging for a common year).

On average, the scatter plots of the daily and monthly averaged data (Fig. 7b) show substantial reduction of the incomplete SEB imbalance as compared with the half-hourly averages. However, imbalances between the turbulent fluxes and the available energy may be worse at daily timescales (cf., Leuning et al., 2012), and in a select number of cases still occur in the monthly averages (cf., Reed et al., 2018), implying some processes extend beyond daily and

monthly timescales. In the next sub-section, we consider some of the factors leading to these biases.

#### 4.3. SEB over different types of soil surfaces

In this sub-section we consider the incomplete SEB and the surface energy fluxes over the entire field campaign at half-hour and longer averaging time scales separately for the three soil conditions identified in Section 4.1. Figure 8 shows scatter plot of the turbulent flux terms in Eq. (1) versus  $R_{net}$  at half-hourly resolution observed from 24 June 2016 to 01 May 2017 for three different soil surfaces (dry, wet, and frozen). Recall also that the soil heat flux,  $G$ , which was not measured, is not used here for the SEB closure analysis (e.g., in Figs. 7 and 8). The turbulent fluxes of the sensible and latent heat shown in Fig. 8a, b increase systematically with increasing net radiation because  $R_{net}$  is normally the principal source of energy for daytime warming of the surface and evaporation. We note different slopes of the bin-averaged fluxes (solid lines) for different soil conditions. According to Fig. 8a, the bin-averaged dependence of  $H_S$  is generally steeper for drier than for wetter soils, whereas the situation with  $H_L$  is obviously opposite; the latent heat flux is small over dry soil surfaces indicating that evaporation is negligible (Fig. 8b). Note also that sensible and latent heat fluxes are comparable over wet soil surfaces (cf. Figs. 8a and 8b) and the Bowen ratio  $Bo = H_S/H_L$  averaged around 1 during daytime (not shown). The different behavior of the turbulent fluxes in Fig. 8 for different soil conditions is perhaps due to the different physical properties of the soils. It can be assumed that wet and/or water-saturated soils, which have larger heat storage due to high specific heat capacity and higher thermal conductivity, cause the observed behaviour of  $H_S$  and  $H_L$  versus

$R_{net}$  (Fig. 8a and 8b). If the soil surface is frozen, both  $H_S$  and  $H_L$  are small and highly variable as mentioned earlier (cf. Fig.6).

According to the bin-averaged data in Fig. 8c, the sum  $H_S + H_L$  is further from closure for wet soils compared to dry soils. The statistical dependence of the turbulent fluxes and  $R_{net}$  for frozen soil surfaces appears weak, if not non-existent (Fig. 8c). As mentioned in Section 4.1, during the cold season topsoil temperatures remain close to 0°C and the soil heat flux term in Eq. (1)  $G = 0$  for an extended period of time. This isothermal freezing process is referred to as the "zero-curtain" effect (e.g., Grachev et al. 2018). Under such conditions, the latent heat of fusion term must be added to Eq. (1). The nature of this term is associated with the change between the liquid and solid phases, as when water turns to ice. The absence of the latent heat of fusion term in the SEB equation explains why Eq. (1) doesn't work for the case of frozen soil surfaces as shown in Fig. 8c. However, a detailed discussion of the SEB during the zero-curtain period is beyond the scope of this paper.

The linear regression forced through the origin (not shown) for the dry soil data shown in Fig. 8c is  $y = 0.79x$ ; that is, the SEB imbalance is 21% in this case. For wet soils over the entire field campaign (Fig. 8c), the linear regression forced through the origin is  $y = 0.72x$ , implying that there is an imbalance of 28%, which is high but not unusual. The linear regression of Fig. 8c for the frozen (snow covered) soil surfaces is  $y = 0.096x$ , implying a weak correlation between the turbulent fluxes and the net radiation. Thus, the surface energy balance in the form of Eq. (1) cannot be applied to freezing soil surfaces without the inclusion of a latent heat of fusion term.

Our results for the SEB closure over dry and wet soils are consistent with prior studies. According to Roxy et al. (2014), SEB closures were lower when the latent heat fluxes were highest, mainly during wet periods; the mean SEB closure was found to be 0.742 and 0.795 for

wet and dry seasons, respectively. Cuxart et al. (2015) reported that very large imbalances are related to high values of soil moisture, especially in warm conditions. However, a multi-year analysis of the surface energy balance in a semi-arid savanna ecosystem in South Africa by Majozi et al. (2017) revealed a SEB closure of  $0.93 \pm 0.11$  with the dry season having the highest energy imbalance (0.70) while the mean SEB closure during the wet season was 1.12.

Figure 9 shows that increasing the averaging time from half-hourly to daily and longer time intervals substantially reduces the SEB imbalance for each soil type (though with some reservations for the frozen soils). For dry soils in Fig. 9a, the linear regression for daily averages forced through the origin is  $y = 0.92x$  and the SEB can be closed within one percent on a seasonal timescale (red six-pointed star). For wet soils (Fig. 9b), the linear regression of daily averages is  $y = 0.79x$  and the SEB closure is  $\approx 0.95$  at a seasonal timescale. For frozen soil surfaces (Fig. 9c), the SEB closure is  $\approx 0.06$  at daily timescales and  $\approx 0.34$  at a seasonal timescale.

Although, increasing the averaging time from half-hourly (Fig. 8c) to daily and longer time intervals (Fig. 9) consistently reduces the SEB imbalance in general for each specific soil condition, the situation is not so obvious if we compare the SEB imbalance between different soil types. For example, the SEB closure at half-hourly resolution for dry soils ( $\approx 0.79$ ) may be approximately the same as the SEB closure for wet soils ( $\approx 0.79$ ) at longer (daily) timescales. In addition, the SEB imbalance may be worse at monthly timescales for wet ( $\approx 0.86$ ) and frozen ( $\approx 0.19$ ) soils compared to daily averages ( $\approx 0.92$ ) for dry soils. Thus, our results support and clarify previous findings by Leuning et al. (2012) and Reed et al. (2018) where in a select number of cases, increasing the averaging time does not always lead to reduction of the SEB imbalance because SEB closures were compared for different sites or different seasons.

#### 4.4. Case studies: the uninterrupted time series ("golden files")

In the previous sections, we considered the incomplete SEB imbalance based on measurements over the entire WFIP 2 field campaign (311-day dataset from 24 June 2016 to 01 May 2017) with and without separation into the three different soil conditions identified in Section 4.1. However, the original in situ data often contain gaps, from very short (half-hour to few hours) up to relatively long (few weeks, Figs. 3-7). Occasional gaps in the data time series are mainly due to equipment failures, calibrations and maintenance operations or general system breakdown. Data quality assurance/control procedures lead to the rejection of "bad" data, generating additional gaps in the data records. For example, turbulent data were edited for spikes, unfavorable relative wind directions, non-stationarity, etc. Averaging of the fragmented data sets raises issues in the interpretation of the results. Gap-filling techniques are commonly used to estimate the missing data; for example, short gaps in data can be filled by interpolation. However, a gap-filling procedure replaces missing empirical data by simulated synthetic values that can introduce more errors.

To overcome these limitations, we consider the longest available uninterrupted time series of relatively good data for each soil condition defined in Section 4.1 ("golden files"). Figures 10-12 show continuous monthly (30-day long) records of the SEB components for dry, wet, and frozen soils respectively. From data in Figs. 10-12, the mean incomplete SEB closure (the slope of a linear regression line with forced origin) for half-hourly averaged data is  $\approx 0.80$  for the dry soils ( $N = 1405$ ),  $\approx 0.73$  for wet soils ( $N = 1201$ ), and  $\approx 0.12$  for frozen soils ( $N = 988$ ). Note that the number of the half-hourly averaged data points in the case of dry (Fig. 10),

wet (Fig. 11), and frozen (Fig. 12) soils is less than the maximum amount possible for one month ( $N = 1440 = 48 \times 30$ ) due to quality control. For daily averages the mean incomplete SEB closure is  $\approx 1.02$ ,  $\approx 0.82$ , and  $\approx 0.22$  for dry (Fig. 10), wet (Fig. 11), and frozen (Fig. 12) soils respectively ( $N = 30$  for each soil type). Thus, the incomplete SEB can be closed for the dry soil within about two percent on a daily timescale for "golden files" data in Fig. 10. Further, the mean incomplete SEB closure based on the one-month averages for the data in Figs. 10-12 are  $\approx 1.06$  (dry soil),  $\approx 0.86$  (wet soil), and  $\approx 0.19$  (frozen soil). Thus, the results based on the almost uninterrupted 30-day time series of fluxes ("golden files", Figs. 10-12) support our previous findings derived from the data collected during the entire 311-day field campaign (gapped time series). That is: (i) increasing the averaging time from half-hourly to daily and monthly intervals generally reduces the incomplete SEB imbalance for specific type of soil; and (ii) the incomplete SEB closure is lower for the wet soils compared to dry soils (e.g., 0.73 vs. 0.80 respectively at half-hourly resolution), while closure is only  $\approx 12\%$  for frozen soils, apparently due to the lack of a latent heat of fusion term in (1). One can estimate the missing latent heat of fusion term in (1) should be  $\approx 0.8$ - $0.9$  of  $R_{net}$  to close the SEB during the cold season.

As expected, the SEB flux components and the topsoil temperature difference series have a pronounced diurnal cycle (rising and falling patterns) for both dry and wet soils (Figs. 10 and 11), whereas for frozen soils (Fig. 12) such a cycle is much less evident (with some exceptions of the net radiation, Fig. 12a). On the diurnal time scale, variations in the turbulent heat fluxes are dominantly forced by daily rhythms in the incoming solar radiation, which also drives changes in the air and soil temperatures. Furthermore, diurnal variations of the residual energy are also observed for both dry (Fig. 10c) and wet (Fig. 11c) soils. According to Figs. 10c and 11c, the daily patterns of the residual energy are characterised by positive values during the first part of

the day and by a sign reversal in the second half of the day. Thus, the observed daily patterns of the residual energy (Figs. 10c and 11c) confirm that the SEB is more easily balanced at daily averaging timescales than half-hourly because of the cancellation of energy residuals of opposite sign. The diurnal variations of the residual energy reported here (Figs. 10c and 11c) are generally in good agreement with previously published results (e.g., Lamaud et al. 2001; Cava et al. 2008; Higgins 2012). The difference of the soil temperature between 10 cm and 5 cm levels for dry, wet, and frozen soils is shown in Figs. 10d, 11d, and 12d respectively. This temperature difference is ultimately related to the ground heat flux  $G$  through Eq. (8). In general, the diurnal cycle of solar radiation modulates a sinusoidal variation of the temperature difference in top soil layer (Figs. 10d and 11d) and, therefore, the ground surface heat flux and diurnal temperature waves. Thereby, much of the energy that enters the soil during the day returns to the atmosphere at night through terrestrial longwave radiation. For this reason,  $G$  is often the smallest component of the daily surface energy balance (solid blue lines in Figs. 10d and 11d). The near-zero temperature difference in the top soil layer during the freezing period (Fig. 12d) is associated with near isothermal temperatures at or around 0°C (zero soil heat flux) and the "zero-curtain" effect as discussed in Sub-section 4.1 earlier.

Figure 13 summarizes the incomplete SEB closure equation (without the ground heat flux  $G$ ) at different temporal scales discussed in Sub-sections 4.2-4.4. The red symbols and lines in Fig. 13 represent all measurements. The SEB imbalance categorized by soil condition are shown in Fig. 13 as green symbols and green dash line (dry soils), blue symbols and blue dash line (wet soils), and cyan symbols and cyan dash line (frozen soils), respectively. The averaged SEB values plotted on this graph for three different soil types are derived from the entire 311-day field campaign except the monthly averages that are based on the uninterrupted 30-day time series for

each type of soil shown in Figs. 10-12 ("golden files"). Averaging operator  $\langle \dots \rangle$  in Fig. 13 denotes the arithmetic mean of the all available original 30-min surface energy fluxes through temporal averaging for a specific timescale (daily, weekly, monthly, seasonal and sub-annual). Figure 13 is the visual representation of our primary findings; that is, increasing the averaging time consistently from half-hourly to longer time intervals substantially reduces the SEB imbalance and the closure is lower for the wet soils as compared to dry soils whereas the SEB closure for frozen soils is very poor, if not non-existent.

#### 4.5. Soil heat flux evaluation at different temporal scales

The purpose of this study is not to investigate closure of the SEB at standard half-hourly time scales (or forcing SEB closure based on the direct measurements of all SEB components mentioned in Section 2). Instead, in this study we evaluate SEB closure over a range of timescales from half-hourly to daily, monthly, seasonal and even sub-annual averaged timescales based on the available direct measured fluxes  $H_S$ ,  $H_L$ , and  $R_{net}$ . In other words, we consider the SEB closure at long time intervals (up to annual timescales) through temporal averaging of the original 30-min data. These time intervals are substantially longer daily averages than those considered in many previous studies (see Section 4.2). In this section we consider estimates of the soil heat flux  $G$  in (1) and its impact on the SEB closure at different temporal scales.

As mentioned earlier, we do not have direct measurements of the soil heat flux during the WFIP 2 field campaign. Moreover, directly measuring  $G$  is a challenging problem in general. Thus, there are numerous approaches to compute the soil heat flux, that use different input data from in situ measurements (e.g., see Liebethal et al. 2005; Liebethal and Foken 2007; Gao et al.

2017b; Yang and Wang 2008 and references therein). Different methods for evaluating  $G$  can use various in situ measurements such as soil temperature, soil moisture, net radiation, etc. In addition, some parameterization approaches can be suitable for different times of the day. The most common approach for determining  $G$  is the calorimetric method (e.g., Liebethal et al. 2005). Some other approaches proposed  $G$  as a simple fraction (linear or nonlinear function) of the net radiation (e.g., Gao et al. 2017b and references therein). Liebethal and Foken (2007) reviewed six different parameterization approaches for  $G$  and compared those with the calorimetric method. In a later study, Gao et al. (2017b) evaluated nine different methods for calculating the soil heat flux at the surface ( $z = 0$ ) by comparing the calculated and measured soil heat flux at 5 cm depth. In this section, we use a traditional calorimetric approach for determining  $G$  at the interface (e.g., Liebethal and Foken 2007, Section 3.1; Gao et al. 2017b, Section 2.1), which combines the flux measurements (by a flux plate) or estimations (from Eq. (8)) at some reference depth  $\Delta z$  below the surface and the calorimetry (estimation of the change in heat storage in the layer between the surface and the depth  $\Delta z$ ). Recall that in the current study, we consider the SEB closure at time intervals substantially longer than daily averages, and the soil heat flux is relatively small and, therefore, less important as compared with the turbulent and radiative surface fluxes at these scales. However, we estimated  $G$  based on the available information to evaluate the influence of  $G$  at different temporal scales.

Here, we use measurements of soil temperature and moisture to estimate  $G$  in (1) based on the Fourier's Law of Heat Conduction (8). We can integrate (8) from the interface down to depth  $\Delta z$ , and relate the flux to the difference in the temperature at the interface to the temperature at depth  $\Delta z$ . Near the surface we can linearly approximate  $T(z)$ , so according to the calorimetric method

$$G = \frac{\lambda}{\Delta z} [\theta_0 - T_S(\Delta z)] + \frac{1}{2} \rho_S c_{ps} \frac{\partial T_S}{\partial t} \Delta z \quad (9)$$

where  $\rho_S$  is the soil density and  $c_{ps}$  is the soil specific heat,  $T_S$  is the soil moisture measured at 5 cm depth; that is  $\Delta z = 5$  cm, and  $\theta_0 = T_S(0)$  is the surface (skin) temperature estimated from the upwelling (outgoing) longwave radiation,  $LW_{up}$ , measurements. Subscripts 'zero' and 'S' in (9) denote surface (a value at the interface  $z = 0$ ) and soil reference height values respectively. Based on our data for the entire experimental period, we estimated the thermal conductivity of the soil  $\lambda$  [ $\text{W m}^{-1} \text{K}^{-1}$ ] via

$$\lambda = 0.180 + 1.09 Q_{S5} \quad (10)$$

where  $Q_{S5}$  [vol/vol] is the soil moisture measured at 5 cm depth. Our estimation (10) is consistent with the coefficients for bare soil from Yao et al (2015) model. We have chosen type 'GRA' (Yao et al. 2015, their Table 1), which includes grassland and barren or sparsely vegetated soil (soil at the PS01 tower site is essentially a plowed fallow field with little vegetation). Note that due to the different the thermal conductivity and heat capacity of the soil, the soil heat flux  $G$  of wet soil is significant larger than of dry soil (see Eqs. (9) and (10)).

The results of the SEB closure computations without and with the soil heat flux  $G$  in Eq. (1) at different temporal scales for the entire dataset and separately for dry and wet soils are summarized in Table 1. The SEB closure without  $G$  (ratio of  $H_S + H_L$  to  $R_{net}$ ) is based only on the direct measurements of the surface fluxes and the data presented in Table 1 correspond to values plotted in Fig. 13; that is, the red symbols for entire dataset, the green symbols for dry soils, and the blue symbols for wet soils, respectively. The SEB closure with  $G$  (ratio of  $H_S + H_L + G$  to  $R_{net}$  in Table 1) is based on the direct measurements of  $H_S$ ,  $H_L$ ,  $R_{net}$  and  $G$  modelled by Eq. (9). The case of frozen soil surfaces was not included in Table 1 because the freezing period is associated with zero soil heat flux,  $G = 0$ , (the "zero-curtain" effect as discussed in

Sub-section 4.1 earlier) and, thus, there is no difference in the SEB closure with and without the soil heat flux  $G$ . As expected, taking the soil heat flux into account in the SEB equation substantially reduces the SEB imbalance at the half-hourly time scales. However, the importance of this correction decreases with increasing averaging time from half-hourly to longer intervals (i.e., to daily, monthly, and sub-annual timescales), because energy locally entering the soil in the morning is released in the afternoon and evening; that is, because of the cancellation of the soil heat flux (and other storage terms) of opposite sign. Table 1 also shows that, at all averaging timescales, the SEB closure with  $G$  (as well as without  $G$ ) is lower for wet soils compared to dry soils.

## 5. Concluding Remarks: Summary and Discussion

In this study, we present an analysis of the surface energy budget (SEB) based on field observations from the Columbia River Gorge in areas of complex terrain near Wasco, Oregon, during a 10-month long portion of the WFIP 2 field campaign (e.g., Bianco et al. 2019; Olson et al. 2019; Shaw et al. 2019; Wilczak et al. 2019). Measurements of half-hourly averaged turbulent and radiative fluxes, surface meteorology, and basic soil parameters made at the PS01 site (Figs. 1 and 2) are used to examine the SEB closure (1) for the entire dataset and separately for different soil conditions (dry, wet, and frozen) at various timescales (from half-hourly to sub-annual averages). Note that similar analysis of energy closure variation over different temporal scales in the literature is rare.

We considered (i) the incomplete the energy balance equation,  $H_S + H_L$  versus  $R_{net}$ ; i.e., Eq. (1) without the ground heat flux term  $G$  since direct measurements of  $G$  were not available

(Sub-sections 4.2 and 4.3), and the "complete" SEB closure equation,  $H_S + H_L + G$  versus  $R_{net}$  (Sub-sections 4.5). The incomplete SEB closure equation (without the ground heat flux  $G$ ) is based only on the direct measurements of the surface fluxes  $H_S$ ,  $H_L$ , and  $R_{net}$ ; whereas, the "complete" SEB closure equation (with  $G$ ) is based on the direct measurements of  $H_S$ ,  $H_L$ ,  $R_{net}$  plus modelled  $G$  (indirect estimates based on Eq. (9)). We estimated the soil heat flux  $G$  in Eq. (1) based on the available information (soil temperature and moisture, upwelling longwave radiation) to evaluate influence of  $G$  at different temporal scales for the entire dataset and separately for dry and wet soils (Sub-section 4.5 and Table 1). Including the estimates of the soil heat flux  $G$  in the SEB closure equation substantially reduces the SEB imbalance,  $H_S + H_L + G$  versus  $R_{net}$ , for each specific soil condition as compared to the incomplete the energy balance equation,  $H_S + H_L$  versus  $R_{net}$  especially at half-hourly averaged timescales (Table 1). However, the importance of the soil heat flux decreases at the longer averaging times (from the daily to sub-annual timescales). In addition, to support our findings derived from the gapped time series collected during the entire 311-day field campaign (Sub-sections 4.2 and 4.3), we use the longest available uninterrupted (almost without gaps) 30-day time series of relatively good data ("golden files") for each type of soils (Sub-section 4.4) to overcome limitations associated with the gapped series.

Our estimates of the complete and incomplete SEB closure equation are generally consistent with past eddy-covariance results over land showing that at half-hourly resolution the sum of turbulent fluxes of sensible and latent heat typically under balance the positive net radiation by about 20-30% during daytime and overestimate negative net radiation at night (Fig. 7a). We note that the SEB-imbalance is a longstanding issue in micro-meteorology. However, increasing the averaging time from half-hourly to longer intervals (i.e., to daily, monthly, and

sub-annual timescales) substantially reduces the SEB imbalance (Fig. 7b) and, additionally, the longer averaging times can reduce the influence of instrumental measurement errors (e.g. improper calibration) and sampling uncertainties. We find the SEB can be closed for this site within reasonable limits on seasonal and sub-annual timescales (311-day averaging for the entire field campaign dataset).

At all averaging timescales, the SEB closure was lower for wet soils compared to dry soils while closure for frozen soils appears weak, if not non-existent (Fig. 13), likely due to the lack of a latent heat of fusion term in the SEB equation (1). However, the latent heat of fusion term is not significant at annual (or sub-annual) timescales because, on average, heat absorbed from the atmosphere during the spring thaw is subsequently released during the fall freeze. This is a temporal redistribution of energy in the top soil layer due to the water/ice-phase transition of the annual freeze–thaw cycle. The SEB can be closed for dry soil within about two percent on a seasonal timescale (81-day) over the entire dataset (Fig. 9a, Fig. 13, and Table 1) and even on a daily timescale for month-long uninterrupted data records ("golden files", Fig. 10).

As mentioned earlier, the purpose of this study is not closure of the SEB at half-hourly time scales, but rather, to evaluate SEB closure over a range of timescales. The problem of surface energy imbalance and the individual factors (e.g., storage terms) that lead to the imbalance at half-hourly and hourly time scales has been widely investigated in many studies (e.g., references in Section 2). Here, we analyze and discuss the balance between net radiation and turbulent sensible and latent heat fluxes. Direct measurements of the soil heat flux (by a flux plate) were not available, which may be seen as a disadvantage, but in many numerical climate models only the net radiation and sensible/latent heat fluxes are used to determine the surface temperature. Thus, SEB closure for these fluxes (Fig. 13) is important. Nevertheless, complete

closure is possible at half-hourly and hourly averaged time scales by accurate determination of all SEB components (turbulent, radiative, ground heat fluxes and storage energy terms) and careful attention to all sources of measurement and data processing errors (e.g., Lamaud et al. 2001; Jacobs et al. 2008; Leuning et al. 2012).

## **Acknowledgements**

This work was supported by the National Oceanic and Atmospheric Administration (NOAA) Atmospheric Science for Renewable Energy (ASRE) program and by the U.S. Department of Energy (DoE) DE-EE0007605 interagency agreement that supports DoE FOA DE-FOA-0000984. The University of Notre Dame team was supported by DOE-WFIFP2-SUB-001. HJSF was also supported by NSF grants AGS-1565535 and 1921554. Special thanks go to Prof. Dr. Thomas Foken for the thorough review, critical and helpful comments on improving the manuscript. We also appreciate the constructive comments and suggestions from Dr. Ola Persson.

## References

- Arya P.S., 1988. *Introduction to Micrometeorology*, Academic Press, San Diego, 307 pp
- Bariteau L., Helmig D., Fairall C.W., Hare J.E., Hueber J., Lang E.K., 2010. Determination of oceanic ozone deposition by ship-borne eddy covariance flux measurements. *Atmos. Meas. Tech.* **3**(2): 441–455. <https://doi.org/10.5194/amt-3-441-2010>
- Bianco L., Djalalova I.V., Wilczak J.M., Olson J.B., Kenyon J.S., Choukulkar A., Berg L., Fernando H.J.S., Grimit E.P., Krishnamurthy R., Lundquist J.K., Muradyan P., Pekour M., Pichugina Y., Stoelinga M.T., Turner D.D., 2019. Impact of model improvements on 80-m wind speeds during the second Wind Forecast Improvement Project (WFIP2). *Geosci. Model Dev. Discuss.* <https://doi.org/10.5194/gmd-2019-80>
- Blomquist B.W., Huebert B.J., Fairall C.W., Bariteau L., Edson J.B., Hare J.E., McGillis W.R., 2014. Advances in air-sea CO<sub>2</sub> flux measurement by eddy correlation. *Boundary-Layer Meteorol.* **152**(3): 245–276. <https://doi.org/10.1007/s10546-014-9926-2>
- Cava D., Contini D., Donato A., Martano P., 2008. Analysis of short-term closure of the surface energy balance above short vegetation. *Agric. Forest Meteorol.* **148**(1): 82–93. <https://doi.org/10.1016/j.agrformet.2007.09.003>
- Charuchittipan D., Babel W., Mauder M., Leps J.-P., Foken T., 2014. Extension of the averaging time of the eddy-covariance measurement and its effect on the energy balance closure. *Boundary-Layer Meteorol.* **152**(3): 303–327. <https://doi.org/10.1007/s10546-014-9922-6>
- Cuxart J., Conangla L., Jiménez M.A., 2015. Evaluation of the surface energy budget equation with experimental data and the ECMWF model in the Ebro Valley. *J. Geophys. Res. Atmos.* **120**(D3): 1008–1022. <https://doi.org/10.1002/2014JD022296>.

776 Ezzahar J., Er-Raki S., Marah H., Khabba S., Amenzou N., Chehbouni G., 2012. Coupling soil-  
777 vegetation-atmosphere-transfer model with energy balance model for estimating energy and  
778 water vapor fluxes over an olive grove in a semi-arid region. *Global Meteorol.* **1**(1): e1.  
779 <https://doi.org/10.4081/gm.2012.e1>

780 Finnigan J., 2008. An introduction to flux measurements in difficult conditions. *Ecological*  
781 *Applications*, **18**(6): 1340–1350. <https://doi.org/10.1890/07-2105.1>

782 Finnigan J.J., Clement R., Malhi Y., Leuning R. Cleugh H.A., 2003. A re-evaluation of long-  
783 term flux measurement techniques, Part I: Averaging and coordinate rotation. *Boundary-*  
784 *Layer Meteorol.* **107**(1): 1–48. <https://doi.org/10.1023/A:1021554900225>

785 Foken T., Oncley S.P., 1995. Results of the workshop "Instrumental and methodical problems of  
786 land surface flux measurements". *Bull. Am. Meteorol. Soc.* **76**(7): 1191–1193

787 Foken T., Wimmer F., Mauder M., Thomas C., Liebethal C., 2006. Some aspects of the energy  
788 balance closure problem. *Atmos. Chem. Phys.* **6**(12): 4395–4402. [https://doi.org/10.5194/acp-](https://doi.org/10.5194/acp-6-4395-2006)  
789 [6-4395-2006](https://doi.org/10.5194/acp-6-4395-2006)

790 Foken T., 2008. The energy balance closure problem: An overview. *Ecological Applications*,  
791 **18**(6): 1351–1367. <https://doi.org/10.1890/06-0922.1>

792 Gao Z., Horton R., Liu H.P., 2010. Impact of wave phase difference between soil surface heat  
793 flux and soil surface temperature on soil surface energy balance closure. *J. Geophys. Res.*  
794 **115**(D16): D16112. <https://doi.org/10.1029/2009JD013278>

795 Gao Z., Liu H., Katul G.G., Foken T., 2017a. Non-closure of the surface energy balance  
796 explained by phase difference between vertical velocity and scalars of large atmospheric  
797 eddies. *Environ. Res. Lett.* **12**(3): 034025. <https://doi.org/10.1088/1748-9326/aa625b>

798 Gao Z., Russell E.S., Missik J.E.C., Huang M., Chen X., Strickland C.E., Clayton R., Arntzen E.,  
799 Ma Y., Liu H., 2017b. A novel approach to evaluate soil heat flux calculation: An analytical  
800 review of nine methods. *J. Geophys. Res.* **122**(D3): 6934–6949.  
801 <https://doi.org/10.1002/2017JD027160>

802 Garratt J.R., 1992. *The Atmospheric Boundary Layer*. Cambridge University Press, U.K. 316 pp

803 Grachev A.A., Fairall C.W., Persson P.O.G., Andreas E.L, Guest P.S., 2005. Stable boundary-  
804 layer scaling regimes: the SHEBA data. *Boundary-Layer Meteorol.* **116**(2): 201–235. DOI  
805 [10.1007/s10546-004-2729-0](https://doi.org/10.1007/s10546-004-2729-0)

806 Grachev A.A., Bariteau L., Fairall C.W., Hare J.E., Helmig D., Hueber J., Lang E.K., 2011.  
807 Turbulent fluxes and transfer of trace gases from ship-based measurements during TexAQS  
808 2006. *J. Geophys. Res.* **116**: D13110. <https://doi.org/10.1029/2010JD015502>

809 Grachev A.A., Andreas E.L, Fairall C.W., Guest P.S., Persson P.O.G., 2015. Similarity theory  
810 based on the Dougherty-Ozmidov length scale. *Quart. J. Roy. Meteorol. Soc.* **141**(690A):  
811 1845–1856. <https://doi.org/10.1002/qj.2488>

812 Grachev A.A., Persson P.O.G., Uttal T., Akish E.A., Cox C.J., Morris S.M., Fairall C.W., Stone  
813 R.S., Lesins G., Makshtas A.P., Repina I.A., 2018. Seasonal and latitudinal variations of  
814 surface fluxes at two Arctic terrestrial sites. *Climate Dynamics.* **51**(5-6): 1793–1818.  
815 <https://doi.org/10.1007/s00382-017-3983-4>

816 Higgins C.W., 2012. A-posteriori analysis of surface energy budget closure to determine missed  
817 energy pathways. *Geophys. Res. Lett.* **39**(19): L19403.  
818 <https://doi.org/10.1029/2012GL052918>

819 Jacobs A.F.G., Heusinkveld B.G., Holtslag A.A.M., 2008. Towards closing the surface energy  
820 budget of a mid-latitude grassland. *Boundary-Layer Meteorol.* **126**(1): 125–136.  
821 <https://doi.org/10.1007/s10546-007-9209-2>

822 Kustas W.P., Daughtry C.S.T., 1990. Estimation of the soil heat flux/net radiation ratio from  
823 spectral data. *Agric. Forest Meteorol.* **49**(3): 205–223. [https://doi.org/10.1016/0168-](https://doi.org/10.1016/0168-1923(90)90033-3)  
824 [1923\(90\)90033-3](https://doi.org/10.1016/0168-1923(90)90033-3)

825 Kustas W.P., Daughtry C.S.T., Van Oevelen P.J., 1993. Analytical treatment of the relationship  
826 between soil heat flux/net radiation ratio and vegetation indices. *Remote Sens. Environ.*  
827 **46**(3): 319–330. [https://doi.org/10.1016/0034-4257\(93\)90052-Y](https://doi.org/10.1016/0034-4257(93)90052-Y)

828 Kustas W.P., Norman J.M., Schmugge T.J., Anderson M.C., 2004. Mapping surface energy  
829 fluxes with radiometric temperature. In: D.A. Quattrochi, J.C. Luvall (eds.) *Thermal remote*  
830 *sensing in land surface processes*. Boca Raton, Florida: CRC Press, 2004, p. 205–253.

831 Lamaud E., Ogée J., Brunet Y., Berbigier P., 2001. Validation of eddy flux measurements above  
832 the understorey of a pine forest. *Agric. Forest Meteorol.* **106**(3): 187–203.  
833 [https://doi.org/10.1016/S0168-1923\(00\)00215-X](https://doi.org/10.1016/S0168-1923(00)00215-X)

834 Lettau H., Davidson B., 1957. Exploring the atmosphere's first mile. Vol. I. *Instrumentation and*  
835 *data evaluation*. Pergamon Press, New York.

836 Liebethal C., Foken T., 2007. Evaluation of six parameterization approaches for the ground heat  
837 flux. *Theor. Appl. Climatol.* **88**(1-2): 43–56. <https://doi.org/10.1007/s00704-005-0234-0>

838 Liebethal C., Huwe B., Foken T., 2005. Sensitivity analysis for two ground heat flux calculation  
839 approaches. *Agric. For. Meteorol.* **132**(3-4): 253–262.  
840 <https://doi.org/10.1016/j.agrformet.2005.08.001>

841 Leuning R., van Gorsel E., Massman W.J., Isaac P.R., 2012. Reflections on the surface energy  
 842 imbalance problem. *Agric. Forest Meteorol.* **156**: 65–74.  
 843 <https://doi.org/10.1016/j.agrformet.2011.12.002>  
 844 Long I.F., Monteith J.L., Penman H.L., Szeicz G., 1964. The plant and its environment.  
 845 *Meteorol. Rundsch.* **17**: 97–101  
 846 Majozi N.P., Mannaerts C.M., Ramoelo A., Mathieu R., Nickless A., Verhoef W., 2017.  
 847 Analysing surface energy balance closure and partitioning over a semi-arid savanna  
 848 FLUXNET site in Skukuza, Kruger National Park, South Africa. *Hydrol. Earth Syst. Sci.*  
 849 **21**(7): 3401–3415. <https://doi.org/10.5194/hess-21-3401-2017>  
 850 Mauder M., Foken T., 2006. Impact of post-field data processing on eddy covariance flux  
 851 estimates and energy balance closure. *Meteorologische Zeitschrift.* **15**(6): 597–609.  
 852 <https://doi.org/10.1127/0941-2948/2006/0167>  
 853 Mauder M., Oncley S.P., Vogt R., Weidinger T., Ribeiro L., Bernhofer C., Foken T., Kohsiek  
 854 W., De Bruin H.A.R., Liu H., 2007. The Energy Balance Experiment EBEX-2000. Part II:  
 855 Intercomparison of eddy-covariance sensors and post-field data processing methods.  
 856 *Boundary Layer Meteorol.* **123**(1): 29–54. <https://doi.org/10.1007/s10546-006-9139-4>  
 857 Masseroni D., Corbari C., Mancini M., 2014. Limitations and improvements of the energy  
 858 balance closure with reference to experimental data measured over a maize field. *Atmósfera*,  
 859 **27**(4): 335–352. [https://doi.org/10.1016/S0187-6236\(14\)70033-5](https://doi.org/10.1016/S0187-6236(14)70033-5)  
 860 Meyers T.P., Hollinger S.E., 2004. An assessment of storage terms in the surface energy balance  
 861 of maize and soybean. *Agric. Forest Meteorol.* **125**(1-2): 105–115.  
 862 <https://doi.org/10.1016/j.agrformet.2004.03.001>

863 Nobel P.S., 2009. *Physicochemical and Environmental Plant Physiology*. Fourth Edition,  
864 Elsevier Academic Press, Oxford UK, 582p.

865 Olson J.B., Kenyon J.S., Djalalova I., Bianco L., Turner D.D., Pichugina Y., Chokulkar A., Toy  
866 M.D., Brown J.M., Angevine W., Akish E., Bao J.-W., Jimenez P., Kosović B., Lundquist  
867 K.A., Draxl C., Lundquist J.K., McCaa J., McCaffrey K., Lantz K., Long C., Wilczak J.,  
868 Banta R., Marquis M., Redfern S., Berg L.K., Shaw W., Cline J., 2019. Improving wind  
869 energy forecasting through numerical weather prediction model development. *Bull. Amer.*  
870 *Meteorol. Society*. <https://doi.org/10.1175/BAMS-D-18-0040.1>

871 Oncley S.P., Foken T., Vogt R., Kohsiek W., DeBruin H.A.R., Bernhofer C., Christen A., van  
872 Gorsel E., Grantz D., Feigenwinter C., Lehner I., Liebethal C., Liu H., Mauder M., Pitacco  
873 A., Ribeiro L., Weidinger T. (2007) The energy balance experiment EBEX-2000, Part I:  
874 Overview and energy balance. *Boundary Layer Meteorol.* **123**(1): 1–28.  
875 <https://doi.org/10.1007/s10546-007-9161-1>

876 Panin G.N., Bernhofer C., 2008. Parametrization of turbulent fluxes over inhomogeneous  
877 landscapes. *Izvestiya, Atmos. Ocean. Phys.* **44**(6): 701–716.  
878 <https://doi.org/10.1134/S0001433808060030>

879 Priestley C. and Taylor R., 1972. On the assessment of surface heat flux and evaporation using  
880 large-scale parameters. *Mon. Wea. Rev.* **100**(2): 81–92.

881 Reed D.E., Frank J.M., Ewers B.E., Desai A.R., 2018. Time dependency of eddy covariance site  
882 energy balance. *Agric. Forest Meteorol.* **249**: 467–478.  
883 <https://doi.org/10.1016/j.agrformet.2017.08.008>

884 Roxy M.S., Sumithranand V.B., Renuka, G., 2014. Soil heat flux and day time surface energy  
885 balance closure at astronomical observatory, Thiruvananthapuram, south Kerala. *J. Earth*  
886 *Syst. Sci.* **123**(4): 741–750. <https://doi.org/10.1007/s12040-014-0437-9>

887 Sauer T.J., Hatfield J.L., Prueger J.H., Norman J.M., 1998. Surface energy balance of a corn  
888 residue-covered field. *Agric. Forest Meteorol.* **89**(3–4): 155–168.  
889 [https://doi.org/10.1016/S0168-1923\(97\)00090-7](https://doi.org/10.1016/S0168-1923(97)00090-7)

890 Shaw W., Berg L., Cline J., Draxl C., Djalalova I., Gruit E., Lundquist J.K., Marquis M.,  
891 McCaa J., Olson J., Sivaraman C., Sharp J., Wilczak J.M., 2019. The second Wind Forecast  
892 Improvement Project (WFIP2): General overview. *Bull. Amer. Meteorol. Society.* **100**(9):  
893 1687–1699. <https://doi.org/10.1175/BAMS-D-18-0036.1>

894 Stone R.S., Dutton E.G., Harris J.M., Longenecker D., 2002. Earlier spring snowmelt in northern  
895 Alaska as an indicator of climate change, *J. Geophys. Res.* **107**(D10): 4089.  
896 <https://doi.org/10.1029/2000JD000286>

897 Stoy P.C., Mauder M., Foken T., Marcolla B., Boegh E., Ibrom A., Arain M.A., Arneth A.,  
898 Aurela M., Bernhofer C., Cescatti A., Dellwik E., Duce P., Gianelle D., van Gorsel E., Kiely  
899 G., Knohl A., Margolis H., McCaughey H., Merbold L., Montagnani L., Papale D.,  
900 Reichstein M., Saunders M., Serrano-Ortiz P., Sottocornola M., Spano D., Vaccari F.,  
901 Varlagin A., 2013. A data-driven analysis of energy balance closure across FLUXNET  
902 research sites: The role of landscape scale heterogeneity. *Agric. Forest Meteorol.* **171-172**:  
903 137–152. <https://doi.org/10.1016/j.agrformet.2012.11.004>

904 Su Z., 2002. The Surface Energy Balance System (SEBS) for estimation of turbulent heat fluxes.  
905 *Hydrol. Earth Syst. Sci.* **6**(1): 85–100. <https://doi.org/10.5194/hess-6-85-2002>

906 Sun T., Wang Z.-H., Ni G.-H., 2013. Revisiting the hysteresis effect in surface energy budgets.  
 907 *Geophys. Res. Lett.* **40**(9): 1741–1747. <https://doi.org/10.1002/grl.50385>  
 908 Wilson K., Goldstein A., Falge E., Aubinet M., Baldocchi D., Berbigier P., Bernhofer C.,  
 909 Ceulemans R., Dolman H., Field C., Grelle A., Ibrom A., Law B.E, Kowalski A., Meyers T.,  
 910 Moncrieff J., Monson R., Oechel W., Tenhunen J., Valentini R., Verma S., 2002. Energy  
 911 balance closure at FLUXNET sites. *Agric. Forest Meteorol.* **113**(1-4): 223–243.  
 912 [https://doi.org/10.1016/S0168-1923\(02\)00109-0](https://doi.org/10.1016/S0168-1923(02)00109-0)  
 913 Wilczak J.M., Oncley S.P., Stage S.A., 2001. Sonic anemometer tilt correction algorithms.  
 914 *Boundary-Layer Meteorol.* **99**(1): 127–150. <https://doi.org/10.1023/A:1018966204465>  
 915 Wilczak J.M., Stoelinga M., Berg L., Sharp J., Draxl C., McCaffrey K., Banta R.M., Bianco L.,  
 916 Djalalova I., Lundquist J.K., Muradyan P., Choukulkar A., Leo L., Bonin T., Pichugina Y.,  
 917 Eckman R., Long C., Lantz K., Worsnop R., Bickford J., Bodini N., Chand D., Clifton A.,  
 918 Cline J., Cook D., Fernando H.J.S., Friedrich K., Krishnamurthy R., Marquis M., McCaa J.,  
 919 Olson J., Otarola-Bustos S., Scott G., Shaw W.J., Wharton S., White A.B., 2019. The second  
 920 Wind Forecast Improvement Project (WFIP2): Observational field campaign. *Bull. Amer.*  
 921 *Meteorol. Society.* **100**(9): 1701–1723. <https://doi.org/10.1175/BAMS-D-18-0035.1>  
 922 Yang K., Wang J., 2008. A temperature prediction-correction method for estimating surface soil  
 923 heat flux from soil temperature and moisture data. *Sci. China Ser. D: Earth Sci.* **51**(5): 721–  
 924 729. <https://doi.org/10.1007/s11430-008-0036-1>  
 925 Yao Y., Liang S., Li X., Chen J., Wang K., Jia K., Cheng J., Jiang B., Fisher J.B., Mu Q.,  
 926 Grünwald T., Bernhofer C., Roupsard O., 2015. A satellite-based hybrid algorithm to  
 927 determine the Priestley-Taylor parameter for global terrestrial latent heat flux estimation

928 across multiple biomes. *Remote Sens. Environ.* **165**: 216–233.

929 <https://doi.org/10.1016/j.rse.2015.05.013>

930

931

**Table 1**

The SEB closure without and with the soil heat flux  $G$  in Eq. (1) at different temporal scales for the entire dataset and separately for dry and wet soils. Soil physical composition: silt (73%), sand (14%), and clay (13%).

Averaging timescales	$(H_S + H_L)/R_{net}$			$(H_S + H_L + G)/R_{net}$		
	Entire	Dry	Wet	Entire	Dry	Wet
Half-hourly	0.763	0.786	0.715	0.946	0.983	0.922
Daily	0.852	0.915	0.794	0.948	1.000	0.908
Weekly	0.908	0.939	0.883	0.980	0.998	0.967
Monthly	0.906	1.057	0.859	0.956	0.9828	0.954
Seasonal	0.989	0.9987	0.948	1.001	1.018	0.965
Sub-annual (311 days)	1.020	N/A	N/A	0.953	N/A	N/A

## Figure Captions

Fig. 1. Maps showing the WFIP 2 study area located along the Columbia River Gorge in eastern Oregon and Washington states.

Fig. 2. View of the flux tower and instruments at the WFIP 2 Physics site PS01 during late summer conditions (15 September 2016).

Fig. 3. Time series of (a) wind speed, (b) true wind direction, (c) air temperature, and (d) relative humidity based on the half-hourly raw data for year days 176–487 (24 June 2016–01 May 2017) observed at Columbia River Gorge, OR during WFIP 2 Project (Physics site PS01).

Fig. 4. Time series of (a) soil temperature and (b) soil moisture observed at the WFIP 2 Physics site PS01, (c) rain rate observed near the Wasco State Airport, OR (WCO), and (d) soil types for year days 176–487 (24 June 2016–01 May 2017). The data are based on half-hour averaging.

Fig. 5. Time series of (a) short-wave (SW) downwelling and upwelling radiation, (b) long-wave (LW) downwelling and upwelling radiation, (c) SW balance, LW balance, and net radiation, and (d) albedo for year days 176–487 (24 June 2016–01 May 2017) observed at Columbia River Gorge, OR during WFIP 2 Project. The data are based on half-hour and daily averaging.

Fig. 6. Time series of (a) friction velocity observed at 3 and 10 m, (b) sensible heat flux observed at 3 and 10 m, (c) latent heat (water vapor) flux, and (d) soil types for year days 176–487 (24

June 2016-01 May 2017) observed at Columbia River Gorge, OR during WFIP 2 Project. The data are based on half-hour averaging.

Fig. 7. Scatter plots of the sum of the sensible and latent heat fluxes  $H_S + H_L$  versus the net radiation  $R_{net}$  based on (a) the half-hourly averaged (symbols) and the bin-averaged (solid line) data and (b) the daily, monthly and 311-day (the entire dataset) averaged fluxes for the entire dataset collected at Columbia River Gorge, OR during WFIP 2 Project during year days 176–487 (24 June 2016-01 May 2017).

Fig. 8. Plots of the bin-averaged (solid lines) and 0.5-hr averaged (symbols) turbulent fluxes (eddy-covariance) of (a) sensible heat  $H_S$ , (b) latent heat  $H_L$ , and (c) the sum  $H_S + H_L$  (SEB turbulent flux components) versus the net radiation  $R_{net}$  for dry, wet, and frozen soils observed at Columbia River Gorge, OR during WFIP 2 Project during year days 176–487 (24 June 2016-01 May 2017).

Fig. 9. Plots of the sum of the sensible and latent heat fluxes  $H_S + H_L$  versus the net radiation  $R_{net}$  separately for (a) dry, (b) wet, and (c) frozen (snow covered) soils based on daily averaged fluxes and entire dataset averaging (81, 92, and 58-day averaging in each case respectively).

Fig. 10. One-month (30-day) time series of (a) the net radiation  $R_{net}$ , (b) the sum of the sensible and latent heat fluxes  $H_S + H_L$ , (c) the residual energy  $R_{net} - H_S - H_L$  and (d) difference of the soil temperature between 10 cm and 5 cm levels for dry soils observed at the WFIP 2 Physics site

PS01 during year days 240–270 (27 August–26 September 2016). The data are based on half-hour and daily averaging.

Fig. 11. Same as Fig. 10 but for wet soils observed at the WFIP 2 Physics site PS01 during year days 450–480 (25 March–24 April 2017). The data are based on half-hour and daily averaging.

Fig. 12. Same as Fig. 10 but for frozen (snow covered) soils observed at the WFIP 2 Physics site PS01 during year days 395–425 (29 January–28 February 2017). The data are based on half-hour and daily averaging.

Fig. 13. The incomplete SEB closure equation (without the ground heat flux  $G$ ) at different temporal scales: ratio of turbulent energy fluxes  $H_S + H_L$  to net radiation  $R_{net}$  for the entire dataset (red solid line and red symbols) and separately for different soil types (dry, wet, and frozen) plotted versus averaging time based on the data collected at Columbia River Gorge, OR during WFIP 2 Project.

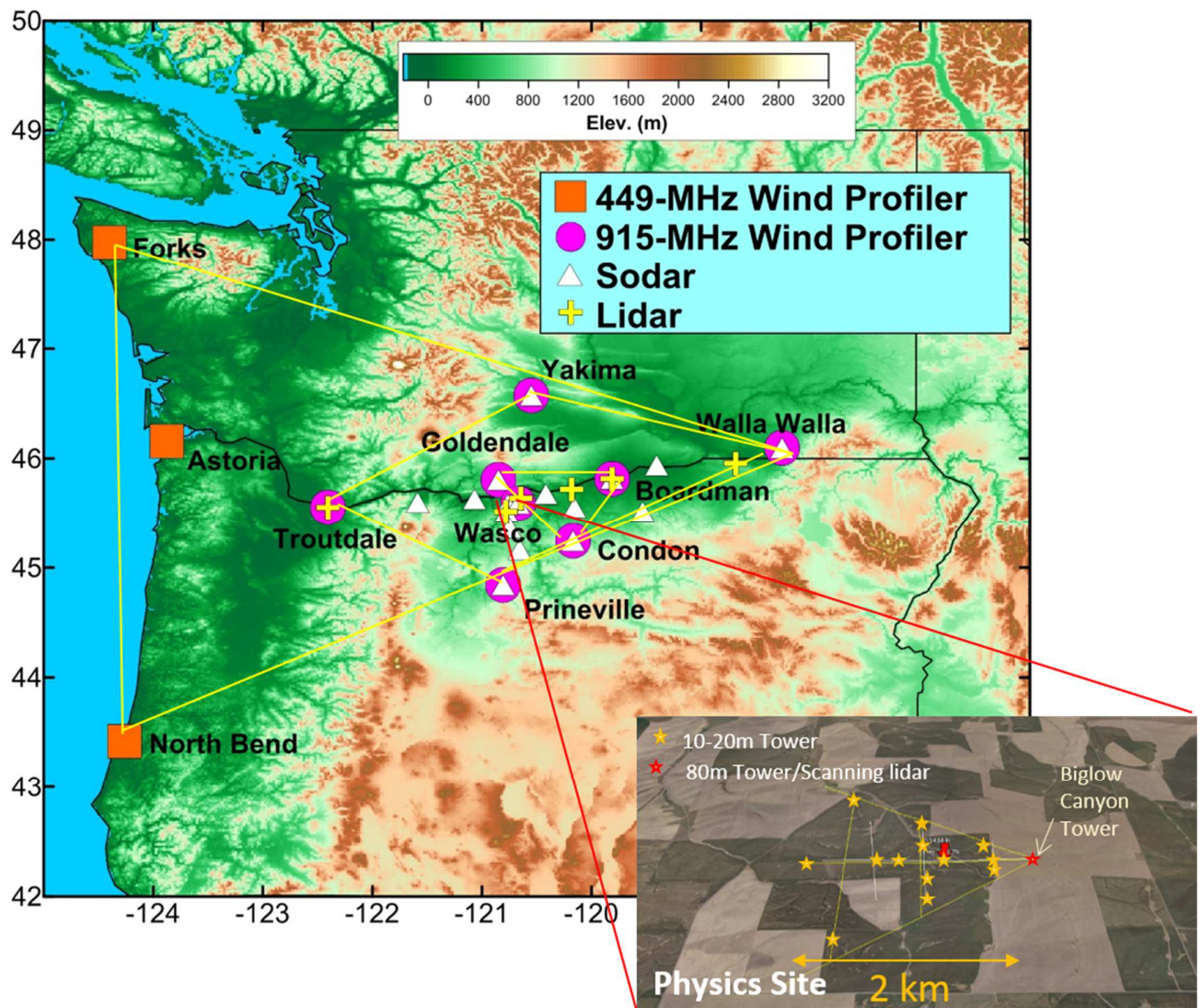


**Fig. 1.** Maps showing the WFIP 2 study area located along the Columbia River Gorge in eastern Oregon and Washington states.



1012

1013

1014 **Fig. 2.** View of the flux tower and instruments at the WFIP 2 Physics site PS01 during late  
1015 summer conditions (15 September 2016).

1016

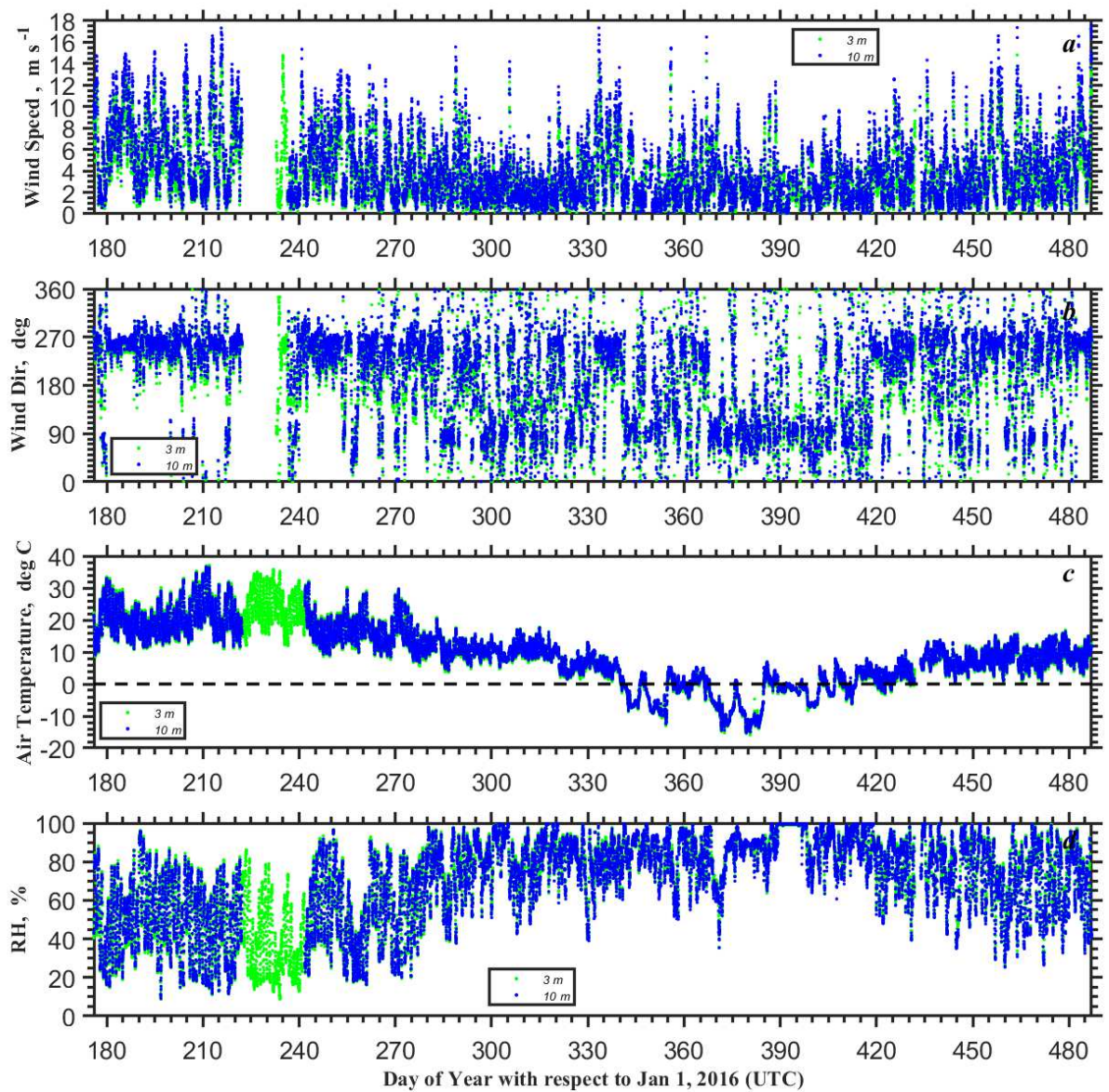


**Fig. 3.** Time series of (a) wind speed, (b) true wind direction, (c) air temperature, and (d) relative humidity based on the half-hourly raw data for year days 176–487 (24 June 2016–01 May 2017) observed at Columbia River Gorge, OR during WFIP 2 Project (Physics site PS01).

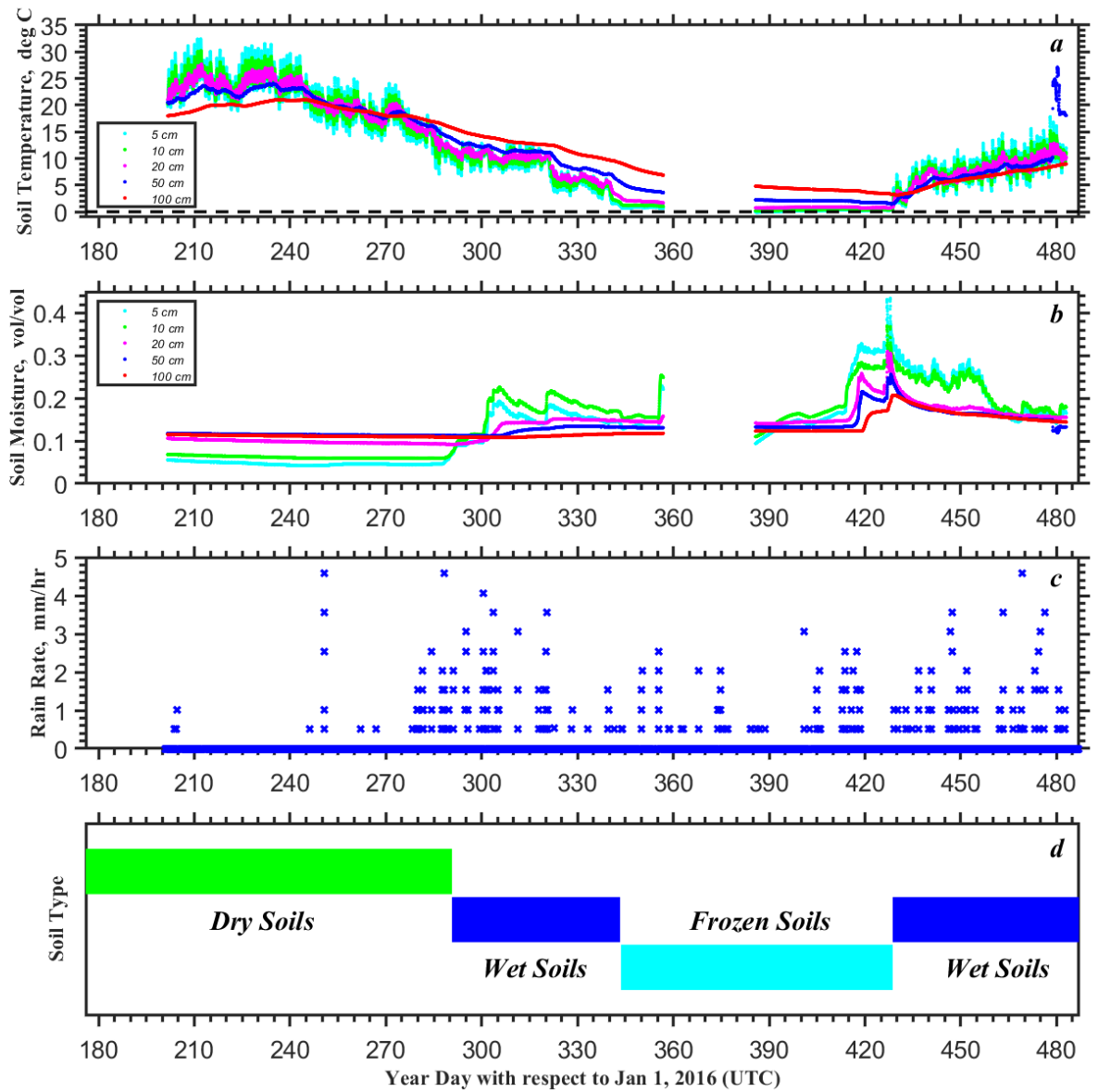


**Fig. 4.** Time series of (a) soil temperature and (b) soil moisture observed at the WFIP 2 Physics site PS01, (c) rain rate observed near the Wasco State Airport, OR (WCO), and (d) soil types for year days 176–487 (24 June 2016–01 May 2017). The data are based on half-hour averaging.

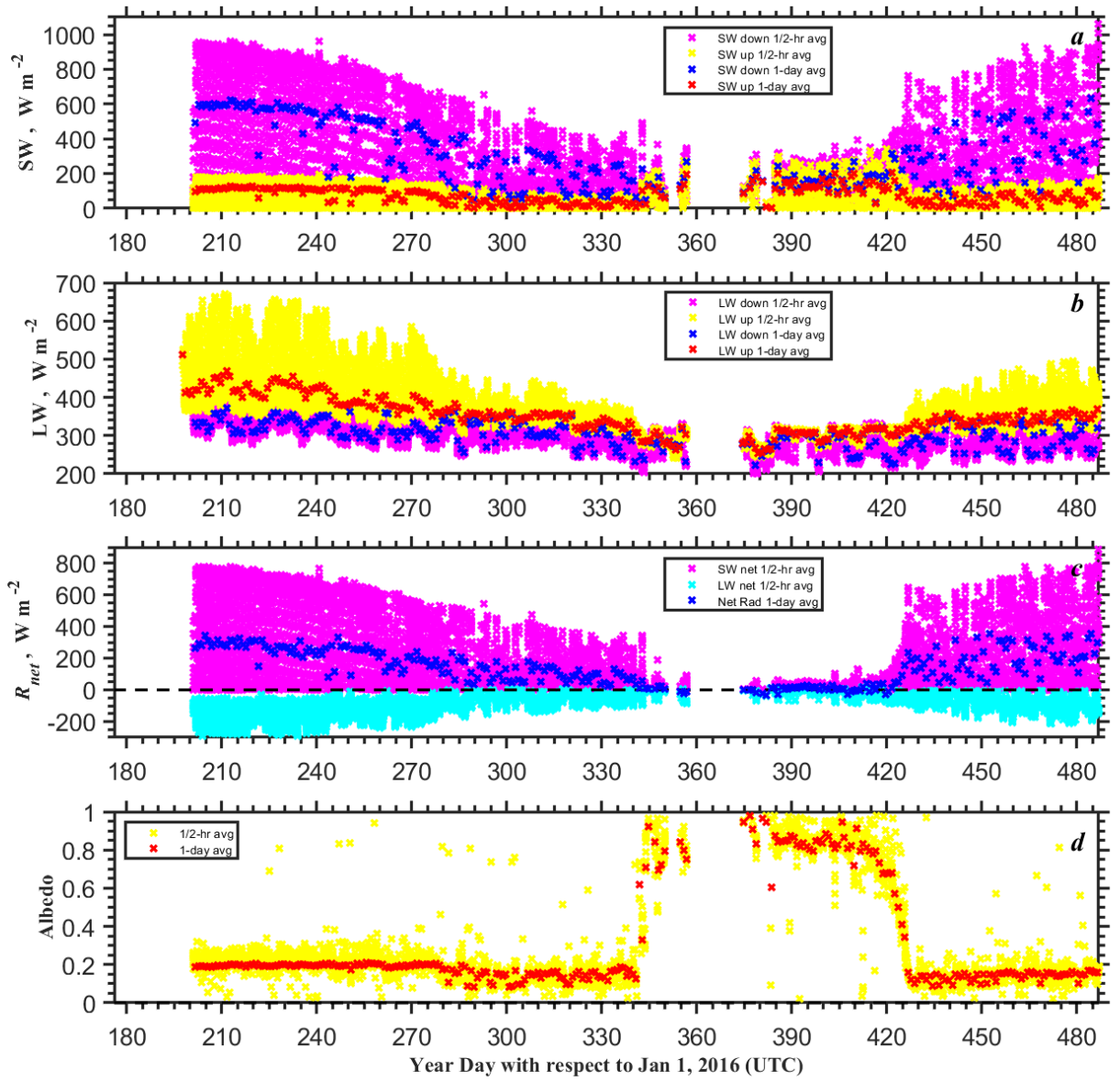


**Fig. 5.** Time series of (a) short-wave (SW) downwelling and upwelling radiation, (b) long-wave (LW) downwelling and upwelling radiation, (c) SW balance, LW balance, and net radiation, and (d) albedo for year days 176–487 (24 June 2016–01 May 2017) observed at Columbia River Gorge, OR during WFIP 2 Project. The data are based on half-hour and daily averaging.

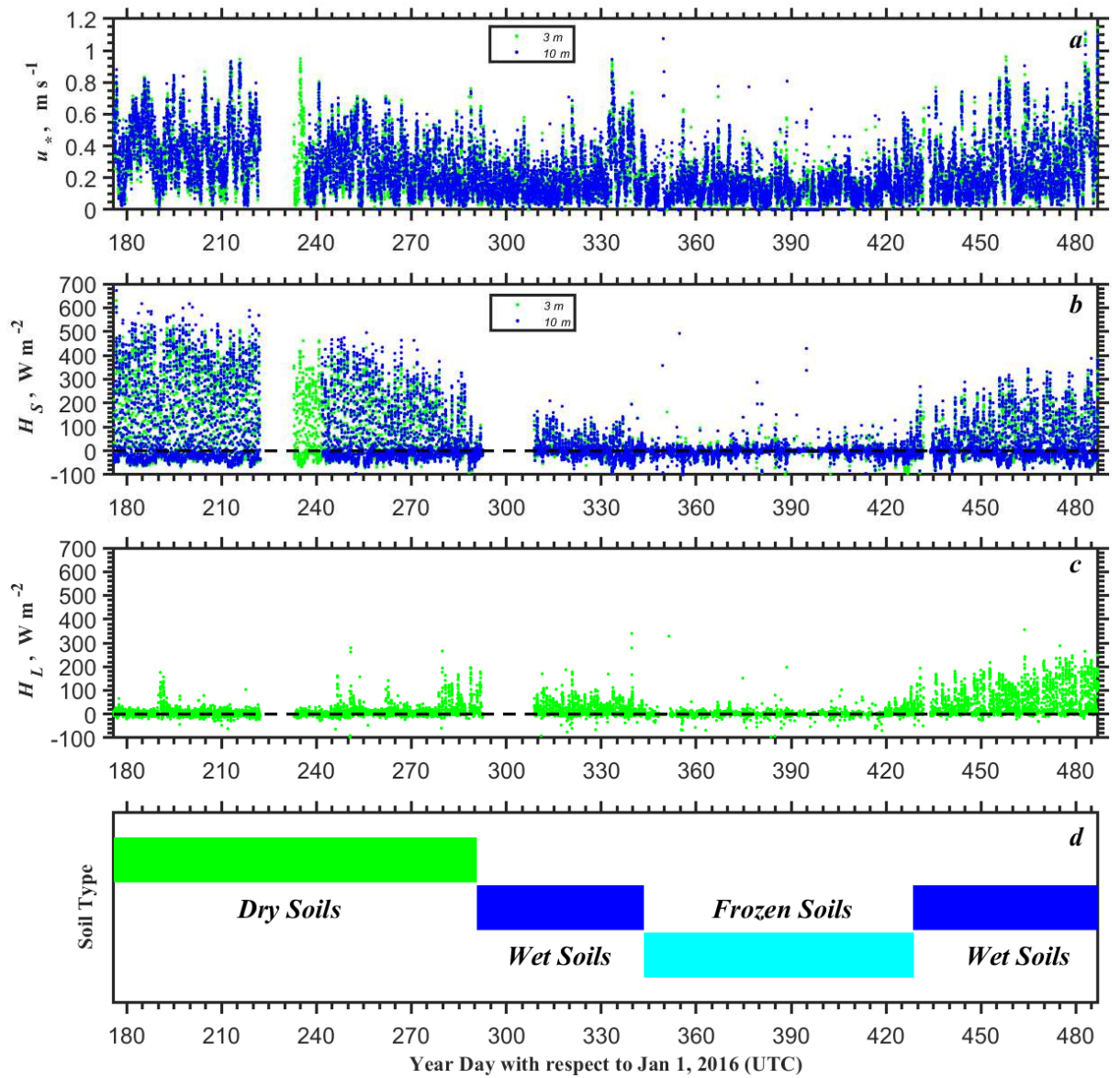


**Fig. 6.** Time series of (a) friction velocity observed at 3 and 10 m, (b) sensible heat flux observed at 3 and 10 m, (c) latent heat (water vapor) flux, and (d) soil types for year days 176–487 (24 June 2016–01 May 2017) observed at Columbia River Gorge, OR during WFIP 2 Project. The data are based on half-hour averaging.

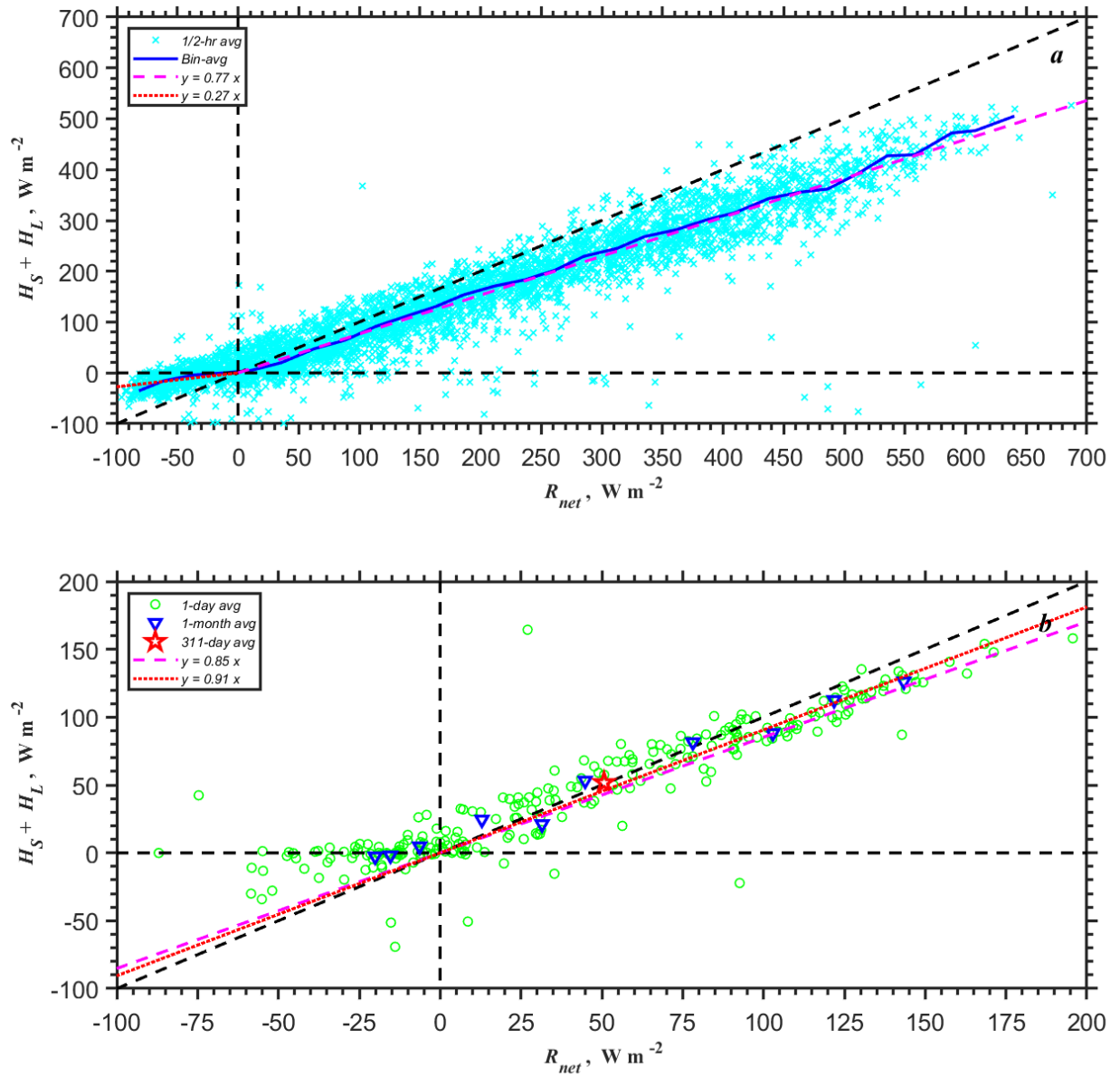


**Fig. 7.** Scatter plots of the sum of the sensible and latent heat fluxes  $H_S + H_L$  versus the net radiation  $R_{net}$  based on (a) the half-hourly averaged (symbols) and the bin-averaged (solid line) data and (b) the daily, monthly and 311-day (the entire dataset) averaged fluxes for the entire dataset collected at Columbia River Gorge, OR during WFIP 2 Project during year days 176–487 (24 June 2016–01 May 2017).

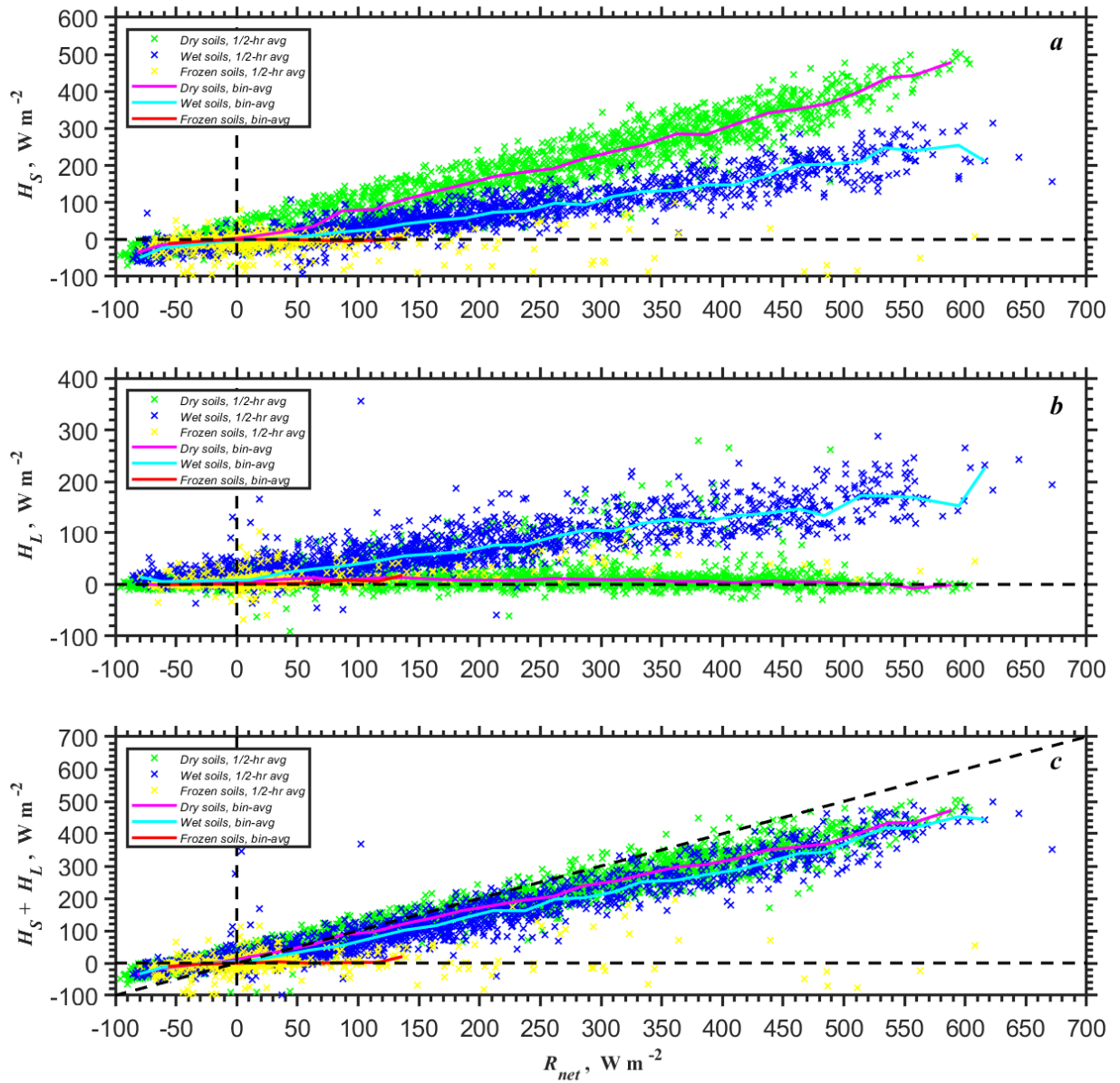
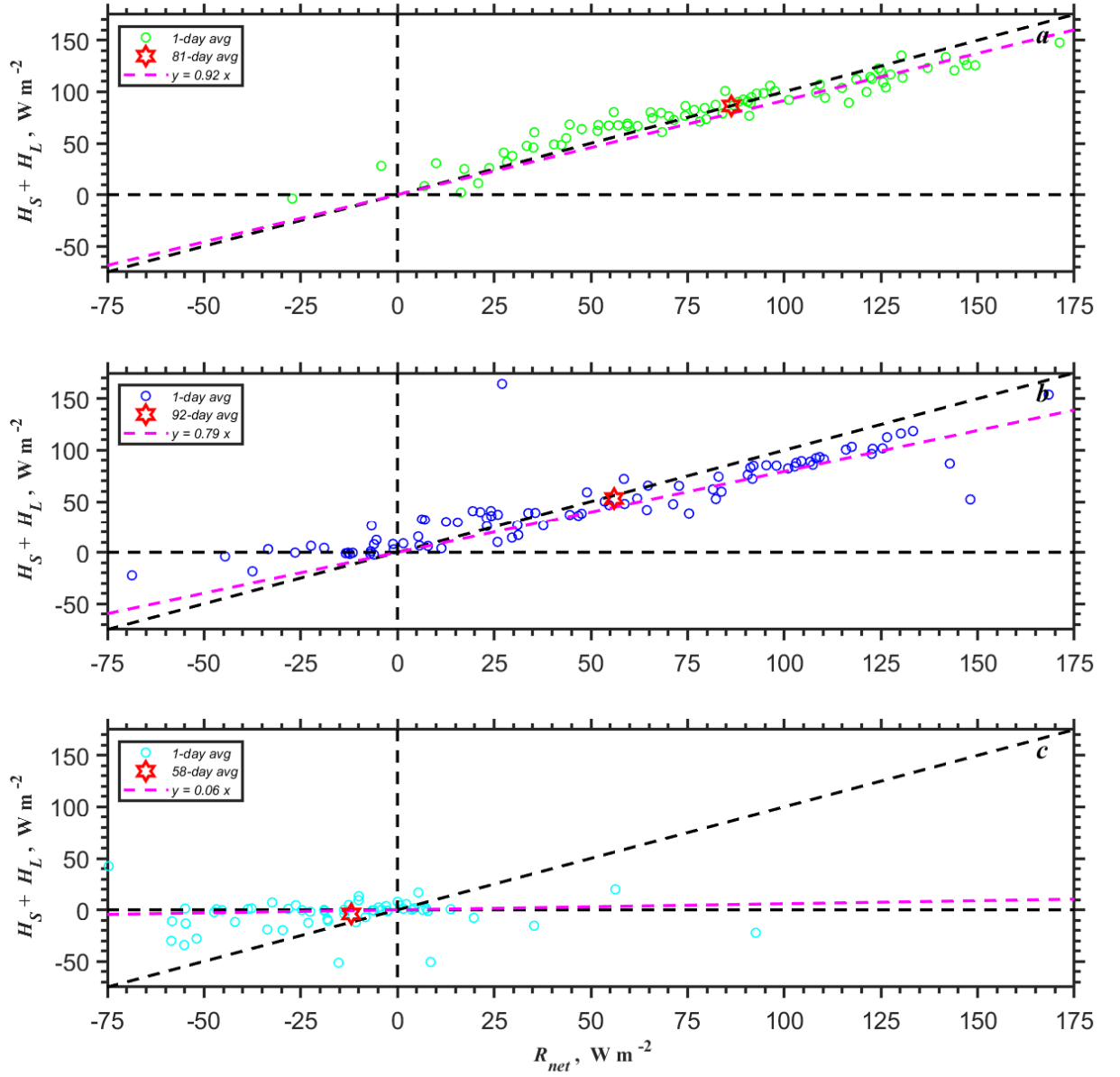


**Fig. 8.** Plots of the bin-averaged (solid lines) and 0.5-hr averaged (symbols) turbulent fluxes (eddy-covariance) of (a) sensible heat  $H_S$ , (b) latent heat  $H_L$ , and (c) the sum  $H_S + H_L$  (SEB turbulent flux components) versus the net radiation  $R_{net}$  for dry, wet, and frozen soils observed at Columbia River Gorge, OR during WFIP 2 Project during year days 176–487 (24 June 2016–01 May 2017).



1050

1051 **Fig. 9.** Plots of the sum of the sensible and latent heat fluxes  $H_S + H_L$  versus the net radiation  
 1052  $R_{net}$  separately for (a) dry, (b) wet, and (c) frozen (snow covered) soils based on daily averaged  
 1053 fluxes and entire dataset averaging (81, 92, and 58-day averaging in each case respectively).

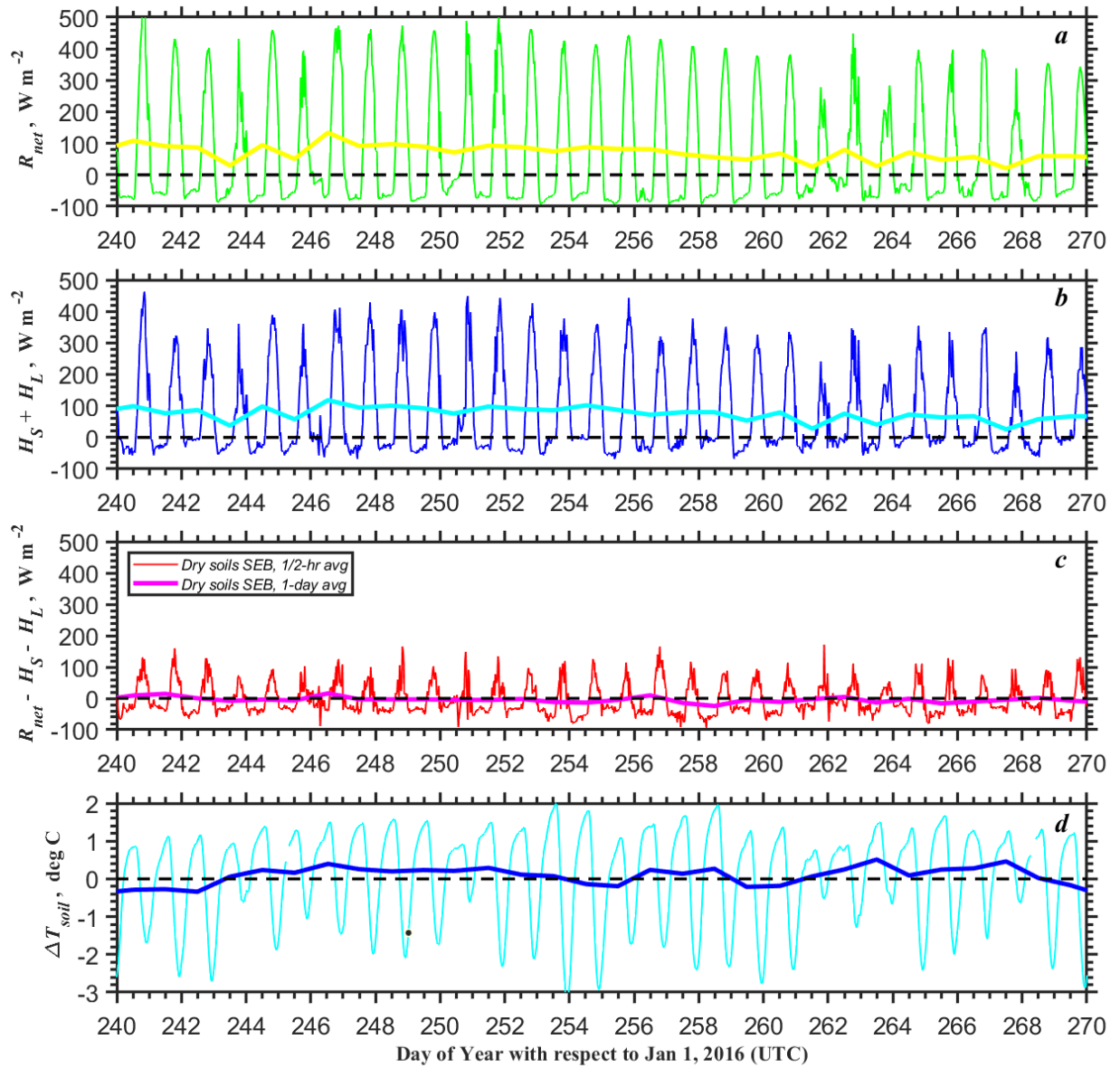


**Fig. 10.** One-month (30-day) time series of (a) the net radiation  $R_{net}$ , (b) the sum of the sensible and latent heat fluxes  $H_S + H_L$ , (c) the residual energy  $R_{net} - H_S - H_L$  and (d) difference of the soil temperature between 10 cm and 5 cm levels for dry soils observed at the WFIP 2 Physics site PS01 during year days 240–270 (27 August–26 September 2016). The data are based on half-hour and daily averaging.

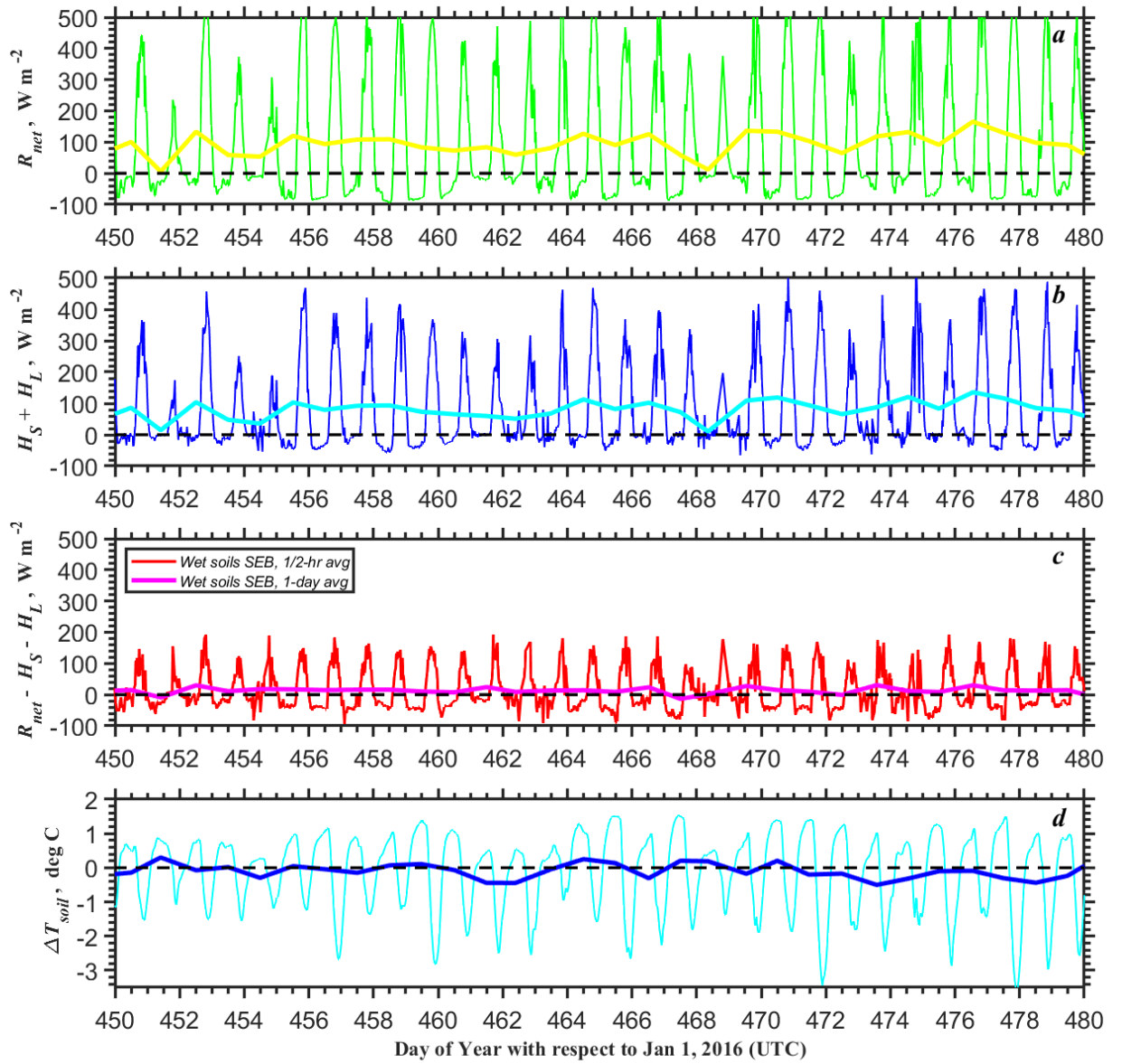


**Fig. 11.** Same as Fig. 10 but for wet soils observed at the WFIP 2 Physics site PS01 during year days 450–480 (25 March–24 April 2017). The data are based on half-hour and daily averaging.

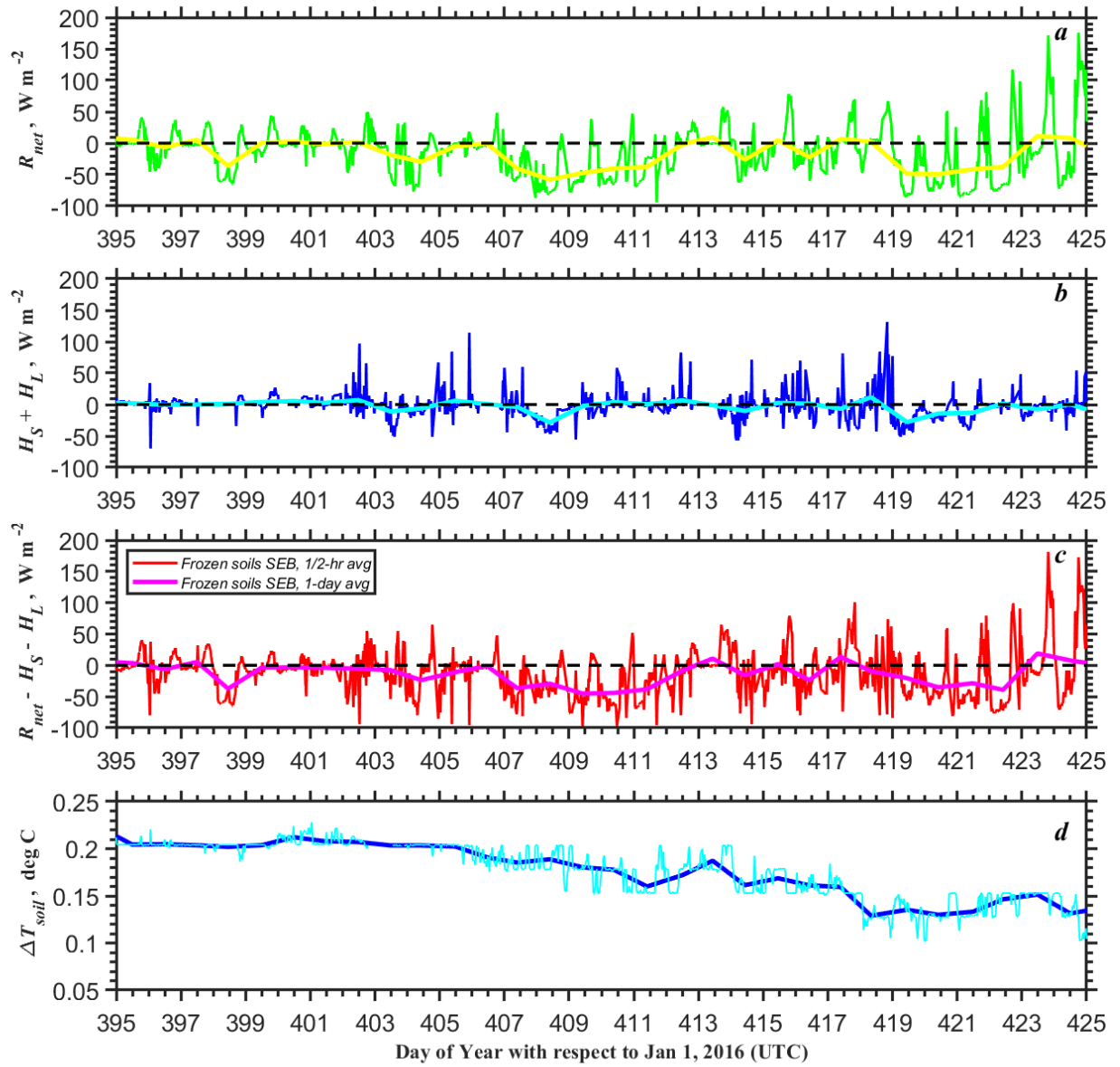


**Fig. 12.** Same as Fig. 10 but for frozen (snow covered) soils observed at the WFIP 2 Physics site PS01 during year days 395–425 (29 January–28 February 2017). The data are based on half-hour and daily averaging.

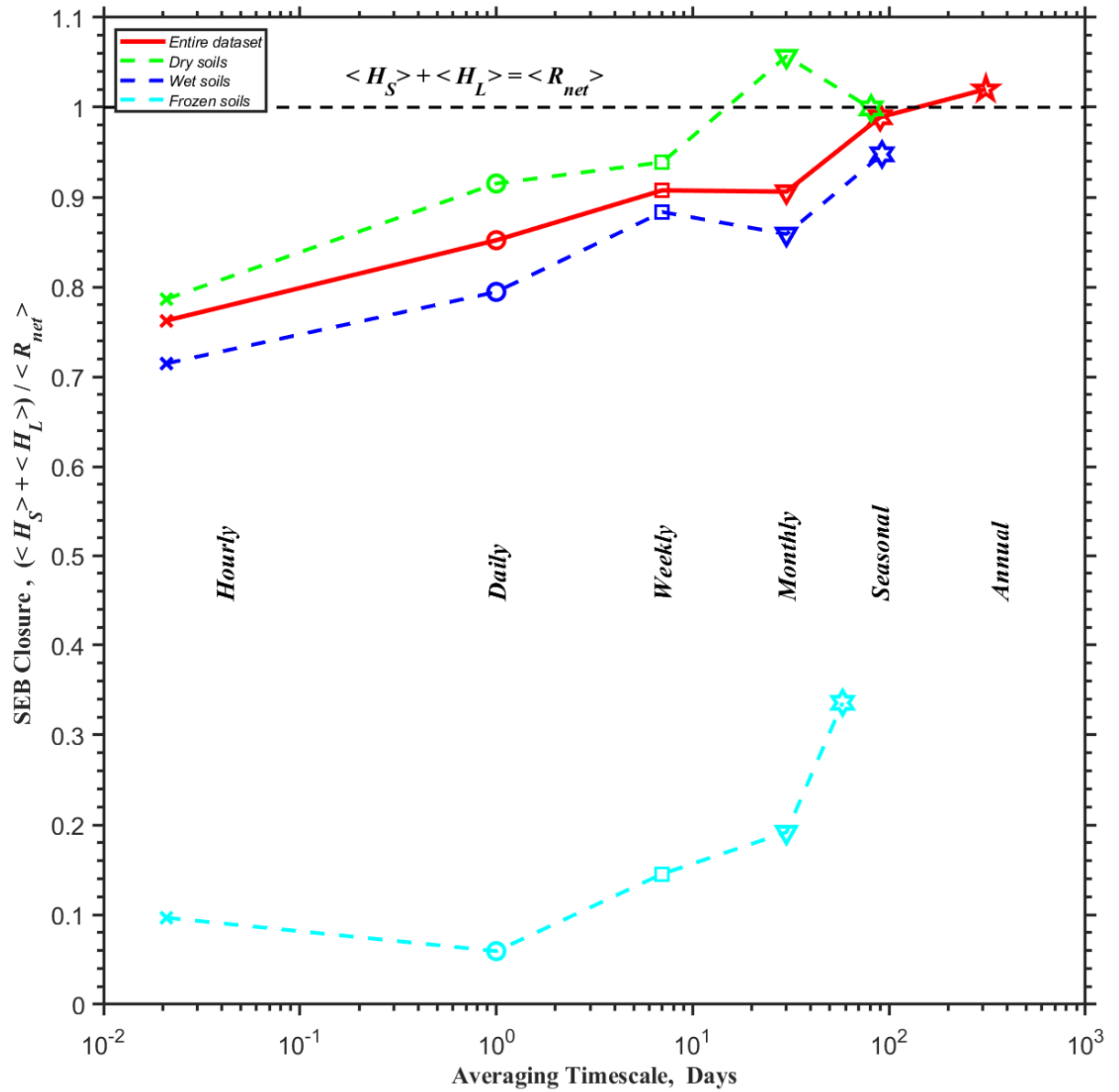


**Fig. 13.** The incomplete SEB closure equation (without the ground heat flux  $G$ ) at different temporal scales: ratio of turbulent energy fluxes  $H_S + H_L$  to net radiation  $R_{net}$  for the entire dataset (red solid line and red symbols) and separately for different soil types (dry, wet, and frozen) plotted versus averaging time based on the data collected at Columbia River Gorge, OR during WFIP 2 Project.